JACS Au
AN OPEN ACCESS JOURNAL OF THE AMERICAN CHEMICAL SOCIETY

pubs.acs.org/jacsau

Article

Deciphering Evolution Pathway of Supported $NO_3^•$ Enabled via Radical Transfer from •OH to Surface NO_3^- Functionality for Oxidative Degradation of Aqueous Contaminants

Jongsik Kim,*[,⊥] Yun Jeong Choe,[⊥] Sang Hoon Kim, In-Suk Choi, and Keunhong Jeong*

Cite This: *JACS Au* 2021, 1, 1158–1177

Read Online

ACCESS | Metrics & More | Article Recommendations | Supporting Information

ABSTRACT: $NO_3^•$ can compete with omnipotent $^•OH/SO_4^{•-}$ in decomposing aqueous pollutants because of its lengthy lifespan and significant tolerance to background scavengers present in H_2O matrices, albeit with moderate oxidizing power. The generation of $NO_3^•$, however, is of grand demand due to the need of $NO_2^•/O_3$, radioactive element, or $NaNO_3/HNO_3$ in the presence of highly energized electron/light. This study has pioneered a singular pathway used to radicalize surface NO_3^- functionalities anchored on polymorphic α-/γ-MnO_2 surfaces (α-/γ-MnO_2-N), in which Lewis acidic $Mn^{2+/3+}$ and NO_3^- served to form $^•OH$ via H_2O_2 dissection and $NO_3^•$ via radical transfer from $^•OH$ to NO_3^- ($^•OH \rightarrow NO_3^•$), respectively. The elementary steps proposed for the $^•OH \rightarrow NO_3^•$ route could be energetically favorable and marginal except for two stages such as endothermic $^•OH$ desorption and exothermic $^•OH$-mediated NO_3^- radicalization, as verified by EPR spectroscopy experiments and DFT calculations. The Lewis acidic strength of the $Mn^{2+/3+}$ species innate to α-MnO_2-N was the smallest among those inherent to α-/β-/γ-MnO_2 and α-/γ-MnO_2-N. Hence, α-MnO_2-N prompted the rate-determining stage of the $^•OH \rightarrow NO_3^•$ route ($^•OH$ desorption) in the most efficient manner, as also evidenced by the analysis on the energy barrier required to proceed with the $^•OH \rightarrow NO_3^•$ route. Meanwhile, XANES and *in situ* DRIFT spectroscopy experiments corroborated that α-MnO_2-N provided a larger concentration of surface NO_3^- species with *bi*-dentate binding arrays than γ-MnO_2-N. Hence, α-MnO_2-N could outperform γ-MnO_2-N in improving the collision frequency between $^•OH$ and NO_3^- species and in facilitating the exothermic transition of NO_3^- functionalities to surface $NO_3^•$ analogues per unit time. These were corroborated by a greater efficiency of α-MnO_2-N in decomposing phenol, in addition to scavenging/filtration control runs and DFT calculations. Importantly, supported $NO_3^•$ species provided 5−7-fold greater efficiency in degrading textile wastewater than conventional $^•OH$ and supported $SO_4^{•-}$ analogues we discovered previously.

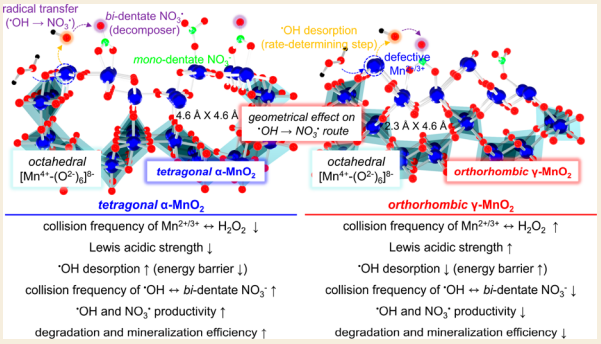

KEYWORDS: *manganese oxide, OH, $NO_3^•$, radical transfer, oxidative degradation, pollutants*

INTRODUCTION

Radical-enabled oxidative fragmentation of aqueous electron (e^-)-rich moieties is primarily dictated by radical's traits such as lifespan (half-life, $t_{1/2}$), electrophilicity (standard reduction potential, E_0), and resistance to background radical scavengers present in H_2O matrices (e.g., HCO_3^-, CO_3^{2-}, Cl^-, etc.).[1,2] $^•OH$ is deemed as an omnipotent radical and exploited due to its large E_0 (2.7 V) yet is short-lived ($t_{1/2}$ of <1 μs) and vulnerable to background scavengers, thereby revealing noticeable efficiencies in degrading contaminants only under a restricted pH span of 3−5.[3−7] Meanwhile, $SO_4^{•-}$ is comparable to $^•OH$ in terms of E_0 (2.6 V), longer-lived ($t_{1/2}$ of ∼35 μsecond), and of a greater tolerance against quenching by backgrounds other than $^•OH$ over a wide pH range.[3,4] Thus, $SO_4^{•-}$ is garnered as an alternative to $^•OH$. As an additional substitute for $^•OH$, $NO_3^•$ has gained attention because of its E_0 (∼2.4 V) and $t_{1/2}$ (∼60 μsecond) along with lesser propensity to accept e^- from background scavengers in comparison with $^•OH$ and $SO_4^{•-}$.[4,8] $NO_2^•$ was reported to react with ozone (O_3) to evolve $NO_3^•$ in the absence of sunlight ($NO_2^• + O_3 \rightarrow NO_3^• + O_2$) yet exhibits a moderate secondary rate constant (k) of 2.1×10^4 M^{-1} s^{-1} and can be viable only after the issues concerning low O_3 solubility in aqueous medium coupled with $NO_2^•$ isolation/transportation are resolved.[9] On the other hand, aqueous NO_3^- can be converted to $NO_3^•$ via pulse radiolysis ($NO_3^- \rightarrow NO_3^• + e^-$),

Received: March 16, 2021
Published: June 23, 2021

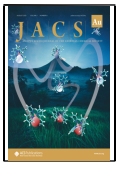

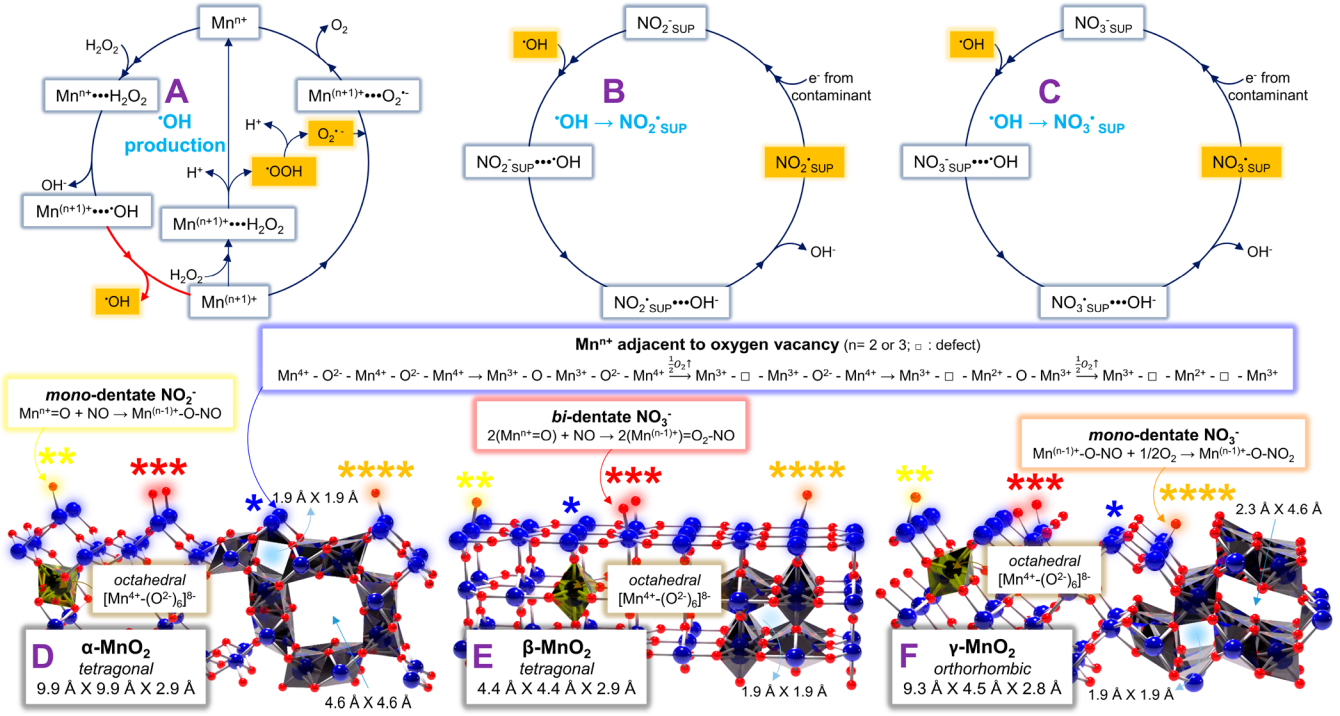

Figure 1. Schematic representation of (A) H_2O_2 scission cycle on surface Mn^{n+} species (n = 2 or 3) and radical transfer from surface-unbound •OH to NO_2^- or NO_3^- species supported on α-/β-/γ-MnO_2 surfaces ($NO_2^-{}_{SUP}$ or $NO_3^-{}_{SUP}$), leading to the production of supported $NO_2^•$ ($NO_2^•{}_{SUP}$ in B) or $NO_3^•$ ($NO_3^•{}_{SUP}$ in C) utilized for degrading aqueous pollutants. Illustration of porous architectures for α-MnO_2 (D), β-MnO_2 (E), and γ-MnO_2 (F), whose surfaces afford NO_2^- or NO_3^- species with various binding configurations. In parts D–F, * denotes defective Mn species accessible to H_2O_2, whereas **, ***, and **** indicate labile O species allowing for the formation of *mono*-dentate NO_2^-, *bi*-dentate NO_3^-, and *mono*-dentate NO_3^- on α-/β-/γ-MnO_2 surfaces.

for which the e^- source should be highly accelerated up to a wavelength of $\leq \sim 10^{-2}$ nm in the presence of a radioactive element (U and Pu).[10,11]

Alternatively, aqueous NO_3^- can be subjected to flash photolysis in the presence of a high-power light source (e.g., excimer ($h\nu$) with a wavenumber (λ) of ~200 nm), leading to the generation of •OH via $NO_3^- + H^+ + h\nu \rightarrow NO_2^• + •OH$.[12,13] In addition, •OH formation is enabled by heterolytic H_2O_2 scission using a Lewis acidic *d*-block metal ion (liquid-phase $M^{\delta+}$; M: metal; δ: 2 or 3) or metal oxide (solid-phase $M^{\delta+}$) as a catalyst, whose details are discussed below.[14] Notably, the resulting •OH produced via catalysis (or photolysis) can radicalize NO_3^- to produce $NO_3^•$ ($NO_3^- + •OH \rightarrow NO_3^• + OH^-$; $•OH \rightarrow NO_3^•$) with a k of 1.4×10^8 M^{-1} s^{-1} (or 5.0×10^5 M^{-1} s^{-1}) utilizing HNO_3 (or $NaNO_3$) as a NO_3^- shuttle.[15,16] The use of HNO_3, however, drastically acidifies the aqueous medium with the pH of 0–1,[15,16] thus tentatively resulting in severe leaching of $M^{\delta+}$ species from a metal oxide. Moreover, the utilization of $NaNO_3$ can release basic Na^+ ions, which poison H_2O_2 activators ($M^{\delta+}$) via coordination.[17,18] Thus, HNO_3 (or $NaNO_3$) can incur only a finite number of utilization for $M^{\delta+}$ species ionized or embedded on metal oxides as H_2O_2 scissors (•OH producer) for activating $•OH \rightarrow NO_3^•$. Indeed, the $•OH \rightarrow NO_3^•$ route is barely deployed because of grand demands on catalytic (or photolytic) •OH evolution.

Nonetheless, NO_3^- is photosensitive and thereby also functions as the precursor of $NO_2^•$ and NO•.[19] In general, NO_3^- is dissociated into NO_2^- ($NO_3^- \rightarrow NO_2^- + 1/2O_2$) or transforms into $NO_2^•$ ($NO_3^- \rightarrow NO_2^• + O^{•-}$) upon $h\nu$ excitation (λ of <250 nm), while evolving •OH ($O^{•-} + H_2O \rightarrow •OH + OH^-$).[19,20] •OH acts as a NO_2^--attacking radical to generate additional $NO_2^•$ via $NO_2^- + •OH \rightarrow NO_2^• + OH^-$ ($•OH \rightarrow NO_2^•$) with a large k of 1.0×10^{10} M^{-1} s^{-1}.[19] However, $NO_2^•$ possesses moderate E_0 (1.0 V) and small $t_{1/2}$ (1.4 μs) and therefore cannot be as efficient as $NO_3^•$ in degrading pollutants.[21,22] Interestingly, NO_2^- experiences further dissection into $O^{•-}$ and NO•.[19] Despite having a lengthy lifetime ($t_{1/2}$ of 10^7 μs), NO• is inactive in degrading contaminants (E_0 of −0.4 V).[23,24] In addition, NO• functions as a •OH sink ($NO• + •OH \rightarrow HNO_2$),[19,25] thereby reducing the probability associated with $NO_2^•$ production via $•OH \rightarrow NO_2^•$. Apparently, the $•OH \rightarrow NO_2^•$ route is kinetically favorable yet imparts $NO_2^•$ with a moderate oxidizing power and is disruptive owing to the presence of NO• used to quench •OH.

Inspection of previous literature concerning $NO_3^•/NO_2^•/NO•$ boosts the preferential usage of $NO_3^•$ as a pollutant degrader over the others and motivates us to envisage a novel route to readily form, sustain, and exploit aqueous $NO_3^•$ under circum-neutral pH and alkali metal-free environments. We previously envisioned a unique •OH → supported $SO_4^{•-}$ ($SO_4^{•-}{}_{SUP}$) pathway under an e^--abundant electric condition, for which SO_4^{2-} functionalities are anchored on *d*-block metal oxide surfaces (e.g., Fe_2O_3, NiO, and Fe-substituted Mn_3O_4) to expedite H_2O_2 scission and radical transfer from •OH to supported SO_4^{2-} ($SO_4^{2-}{}_{SUP}$) via a series of elementary steps (Figure 1A and C).[26−28] Initially, a lone pair of electrons on H_2O_2 bind with Lewis acidic surface $M^{\delta+}$ species (Fe^{2+}, Ni^{2+}, or $Mn^{2+/3+}$) to produce $M^{\delta+}\cdots H_2O_2$ prior to heterolytic H_2O_2 splitting to form surface $M^{(\delta+1)+}\cdots$•OH and surface-unbound $^-$OH (Figure 1A).[26−28] $M^{(\delta+1)+}\cdots$•OH then desorbs •OH, by

https://doi.org/10.1021/jacsau.1c00124
JACS Au 2021, 1, 1158−1177

which $SO_4^{\bullet-}$ productivity via the $^{\bullet}OH \rightarrow SO_4^{\bullet-}{}_{SUP}$ route is directed. This indicates that the $^{\bullet}OH$ desorption stage dominates the overall $^{\bullet}OH \rightarrow SO_4^{\bullet-}{}_{SUP}$ route as the rate-determining step (red arrow in Figure 1A).[26−28] Finally, $M^{(\delta+1)+}$ on the surface is reduced to $M^{\delta+}$ via e^- reduction for the recycling H_2O_2 scission cycle.[26−28] Meanwhile, surface-unbound $^{\bullet}OH$ migrates to and interacts with the $SO_4^{2-}{}_{SUP}$ functionality, undergoing transition from $SO_4^{2-}\cdots{}^{\bullet}OH$ to $SO_4^{\bullet-}\cdots OH^-$ to $SO_4^{\bullet-}$ upon the release of OH^- to the aqueous medium ($SO_4^{2-}/SO_4^{\bullet-}$ in exchange for $NO_3^-/NO_3^{\bullet}$ in Figure 1C).[26−28] $SO_4^{\bullet-}{}_{SUP}$ can radicalize or destabilize contaminant via e^- exchange prior to the recovery of SO_4^{2-} for reactivating radical interconversion of $^{\bullet}OH \leftrightarrow SO_4^{\bullet-}{}_{SUP}$.[26−28] Of note, $^{\bullet}OH \rightarrow SO_4^{\bullet-}{}_{SUP}$ can be activated at circum-neutral pH of 5.5−7.0 with the exclusion of $M^{\delta+}$ poisons (alkali metals).[26−28] Of additional note, $SO_4^{\bullet-}{}_{SUP}$ can outperform conventional $^{\bullet}OH$ in decomposing contaminant via an efficient/recyclable fashion.[26−28]

Herein, we postulated that NO_3^- functionalities can be grafted on a metal oxide in proximity to surface $M^{\delta+}$ species, substitute for SO_4^{2-} functionalities, and activate the $^{\bullet}OH \rightarrow$ supported $NO_3^{\bullet}$ ($NO_3^{\bullet}{}_{SUP}$) route (Figure 1C). It should be stressed that H_2O_2 can be continuously generated and fed to surface $M^{\delta+}/M^{(\delta+1)+}$ species for H_2O_2 scission/$M^{\delta+}$ recovery in the presence of an electric potential.[26−28] Nonetheless, this study rules out the utilization of an electric environment and serves an excess amount of H_2O_2 as $^{\bullet}OH$ precursor to substantiate the tangibility of $^{\bullet}OH \rightarrow NO_3^{\bullet}{}_{SUP}$ by simplifying reaction environments. Moreover, even with the absence of an abundant amount of e^- generated under an electric condition, surface $M^{\delta+}$ species can be readily recovered via alternative pathways.[29,30] For instance, $M^{(\delta+1)+}$ is bound to H_2O_2 to form $M^{(\delta+1)+}\cdots H_2O_2$, which in turn dissects H_2O_2 via e^- donation from H_2O_2 to $M^{(\delta+1)+}$, leading to the recovery of $M^{\delta+}$ with the emission of proton (H^+) and $^{\bullet}OOH$ to aqueous medium (Figure 1A).[29,30] Moreover, $^{\bullet}OOH$ can be further cleaved to H^+ and $O_2^{\bullet-}$. $O_2^{\bullet-}$ is then coordinated to $M^{(\delta+1)+}$ to form $M^{(\delta+1)+}\cdots O_2^{\bullet-}$, where e^- is moved from $O_2^{\bullet-}$ to $M^{(\delta+1)+}$ to recover $M^{\delta+}$ with the liberation of O_2 (Figure 1A).[29,30] Furthermore, H_2O_2 also served in this study to minimize the separation of NO_3^- species from the surface. This is because NO_3^- intrinsically possesses low binding affinity to the surface[31,32] and thereby might be detached easily from the surface if the surface were heated by an electric energy. This raises the need to select the metal oxide proper to afford a large amount of NO_3^- functionalities on its surface. Importantly, given the exothermic nature of $^{\bullet}OH \rightarrow SO_4^{\bullet-}{}_{SUP}$ or $^{\bullet}OH \rightarrow NO_3^{\bullet}$ under aqueous medium,[15,16,26−28] $^{\bullet}OH \rightarrow NO_3^{\bullet}{}_{SUP}$ was presumed to be energetically favorable.

Overall, the surface should favor NO_3^- adsorption and contain a large quantity of Lewis acidic $M^{\delta+}$ species with strengths desired to desorb $^{\bullet}OH$ for lowering the energy barrier of the tentative rate-determining stage for $^{\bullet}OH \rightarrow NO_3^{\bullet}{}_{SUP}$. Mn oxides are classified as one of the reducible oxides with structural flexibility,[33,34] by which Mn^{4+} (or Mn^{3+}) readily accepts e^- from adjacent O^{2-}, liberates oxygen, and transforms into defective, Lewis acidic Mn^{3+} (or Mn^{2+}; Mn^{n+}; n = 2 or 3),[35] as highlighted with the blue box in Figure 1. Mn^{n+} can be in access to H_2O_2 and cleave H_2O_2 to evolve $^{\bullet}OH$. Meanwhile, a portion of the Mn^{n+} species may act as anchoring spots of NO_Y^- (Y = 2 or 3) formed via chemical fusion of NO/O_2 on or near Mn^{n+} species, as reported previously.[36,37] In addition, labile oxygens (O_α) bound to surface Mn^{n+} species are also prone to bind with NO/O_2 and generate NO_2^-/NO_3^- functionalities with *mono-* or *bi*-dentate configuration along with reductive transition of Mn^{n+} to $Mn^{(n-1)+}$.[38,39] (See boxes highlighted with yellow/red/orange in Figure 1.) It should be noted that NO_2^- functionalities can be radicalized via the $^{\bullet}OH \rightarrow NO_2^{\bullet}{}_{SUP}$ route (Figure 1B) yet cannot be desirable in decomposing contaminant due to the demerits of $NO_2^{\bullet}$ stated above.[19,21,22,40] Nevertheless, these can suggest the merits of Mn oxides in activating $^{\bullet}OH \rightarrow NO_3^{\bullet}{}_{SUP}$ and pose the necessity to select the Mn oxide suitable to disperse Mn^{n+}/O_α species with desired properties. Mn species are multivalent in nature ($Mn^{2+}/Mn^{3+}/Mn^{4+}$) and therefore offer a variety of architectures including MnO, Mn_3O_4, Mn_2O_3, and MnO_2, among which MnO_2 was reported to provide the largest quantities of O_α and/or Mn^{n+} species,[41,42] thereby being chosen herein. Notably, MnO_2 offers a series of polymorphs such as α-/β-/γ-/δ-/ε-/λ-MnO_2, wherein δ-/ε-/λ-MnO_2 are metastable under aqueous or ambient environments[43,44] and thus are excluded in this study.

α-/β- and γ-MnO_2 are defined by crystal systems of *tetragonal* and *orthorhombic*, respectively, across which *octahedral* $[Mn^{4+}\text{-}(O^{2-})_6]^{8-}$ motifs could provide H_2O_2-inaccessible Mn^{4+} species only if α-/β-/γ-MnO_2 were defect-free (Figure 1D−F).[41−44] However, polycrystalline α-/β-/γ-MnO_2 can be deformed to possess mesoporosities and ample Mn^{n+}/O_α species,[45,46] whose numbers and strengths are presumably distinct due to the difference in their cell edges, albeit with identical cell angle of 90°. Of interest, α-/β-/γ-MnO_2 bear 1.9 Å × 1.9 Å-sized tunnels inaccessible to H_2O_2, NO_2^-, and NO_3^- (2.3−2.9 Å in Figure 1D−F).[41−46] Of interest, this holds true in β-MnO_2 with a single tunnel of 1.9 Å × 1.9 Å yet should be reconsidered in α-/γ-MnO_2. α- and γ-MnO_2 provides additional tunnels with the sizes of 4.6 Å × 4.6 and 2.3 Å × 4.6 Å, respectively, into which H_2O_2 and NO_3^- can be diffused (Figure 1D−F).[41−46] It may be reasonable to conjecture that α-MnO_2 has pores with the biggest size, is most amicable for H_2O_2 and NO/O_2 to diffuse into Mn^{n+} and O_α species present in the pores, and thus may exhibit the highest efficiencies in producing $^{\bullet}OH$ and $NO_3^{\bullet}$ among α-/β-/γ-MnO_2 considered. The hypothesis stated above, however, could be valid only when the numbers/strengths of Mn^{n+}/O_α species were alike across α-/β-/γ-MnO_2. Of significance, this hypothesis could be coupled with textural traits of α-/β-/γ-MnO_2, which are of challenge to be regulated even post amending synthetic methodologies. This highly suggests that $NO_3^{\bullet}$ productivities on NO_3^--functionalized α-/β-/γ-MnO_2 should be tested under diffusion-free environments and compared in terms of site basis rather than gram or area basis for rigorous comparison.

Again, in order to compensate for the aforementioned demerits of unsupported $^{\bullet}OH/SO_4^{\bullet-}/NO^{\bullet}/NO_2^{\bullet}/NO_3^{\bullet}$ as a decomposer of pollutants, it is necessary to discover a unique yet easy way to produce and sustain $NO_3^{\bullet}$ species. This study first reports the viability and impact of $^{\bullet}OH \rightarrow NO_3^{\bullet}{}_{SUP}$ to generate $NO_3^{\bullet}{}_{SUP}$ deployed for contaminants' degradation, for which α-/β-/γ-MnO_2 serve as platforms to accommodate Mn^{n+}/O_α. α-/β-/γ-MnO_2 and their NO_3^--modified analogues were synthesized for comparison and subjected to spectroscopic analysis (EPR and XANES) and DFT calculations to simulate and corroborate the plausibility of H_2O_2 splitting and $^{\bullet}OH \rightarrow NO_3^{\bullet}{}_{SUP}$. In addition, the catalysts were examined in degrading a model compound of aqueous pollutants (phenol) and/or textile wastewater. Furthermore, the kinetics of $^{\bullet}OH \rightarrow$

https://doi.org/10.1021/jacsau.1c00124
JACS Au 2021, 1, 1158−1177

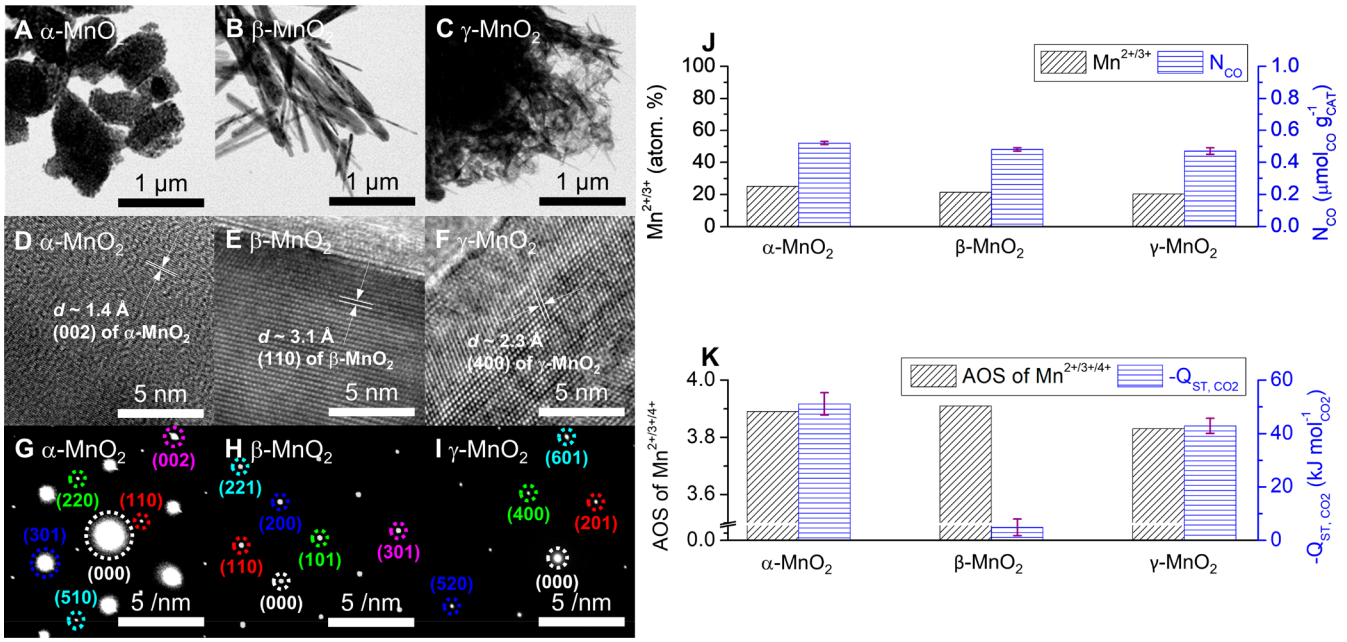

Figure 2. HRTEM images of α-MnO_2 (A and D), β-MnO_2 (B and E), and γ-MnO_2 (C and F). In D−F, lattice fringes with d values of 1.4 Å, 3.1 Å, and 2.3 Å are indexed to (002), (110), and (400) facets for *tetragonal* α-MnO_2 (JCPDF No. of 01-072-1982), *tetragonal* β-MnO_2 (JCPDF No. of 00-024-0735), and *orthorhombic* γ-MnO_2 (JCPDF No. of 01-082-2169), respectively. SAED patterns of α-MnO_2 (G), β-MnO_2 (H), and γ-MnO_2 (I), where dots indicate surface facets assigned to those of α-, β-, or γ-MnO_2. (J) Atomic concentrations of Mn^{2+}/Mn^{3+} species present in or near the catalyst surfaces and the amounts of CO-accessible Mn species included per gram of the catalysts (N_{CO}). (K) Average oxidation states (AOS) of $Mn^{2+}/Mn^{3+}/Mn^{4+}$ species present in or near the catalyst surfaces and the isosteric heats of CO_2 adsorption ($-Q_{ST,CO2}$) for the catalysts at small CO_2 coverages (~5.1 μmol g_{CAT}^{-1} for α-MnO_2 and γ-MnO_2; ~3.7 μmol g_{CAT}^{-1} for β-MnO_2).

$NO_3^{\bullet}{}_{SUP}$ on the catalysts were assessed to elaborate the significance of their geometric differences on the properties of Mn^{n+}, NO_3^-, and $NO_3^{\bullet}$ along with the extraction of kinetic parameters.

RESULTS AND DISCUSSION

Properties of α-/β-/γ-MnO_2

One of our primary goals was to validate the advantages of $^{\bullet}OH \rightarrow NO_3^{\bullet}{}_{SUP}$ on NO_Y^--functionalized α-/β-/γ-MnO_2 (denoted as α-/β-/γ-MnO_2-N; Y= 2 or 3) in degrading aqueous contaminants relative to $^{\bullet}OH$ production on α-/β-/γ-MnO_2. Hence, α-/β-/γ-MnO_2 were first isolated via hydrothermal synthesis, during which multiple, equimolar Mn precursors of Mn^{2+}/MnO_4^- or Mn^{2+} oxidant of $(NH_4)_2S_2O_8$ served to preferentially crystallize α-/β-/γ-MnO_2 architectures at 90−160 °C.[47,48] Porosities of α-/β-/γ-MnO_2 were analyzed via N_2 isotherm techniques, by which α-/β-/γ-MnO_2 were verified to possess diverse BET surface areas (S_{BET}) of 10−160 m^2 g_{CAT}^{-1} and BJH pore volumes (V_{BJH}) of 0.1−0.2 cm^3 g_{CAT}^{-1} with β-MnO_2 being almost nonporous. This suggested that the amounts of Mn^{n+}/O_α species exposed to H_2O_2/NO_Y^- precursor (NO/O_2) were severely limited in β-MnO_2, thereby potentially resulting in the smallest $^{\bullet}OH \rightarrow NO_3^{\bullet}{}_{SUP}$ efficiency on β-MnO_2-N per gram basis. Conversely, α-/γ-MnO_2 showed moderate S_{BET} values of ≥50 m^2 g_{CAT}^{-1} and might have larger quantities of Mn^{n+}/O_α species (NO_Y^--anchoring spot) available to conduct $^{\bullet}OH \rightarrow NO_3^{\bullet}{}_{SUP}$ compared to β-MnO_2. Nevertheless, $^{\bullet}OH \rightarrow NO_3^{\bullet}{}_{SUP}$ efficiencies on α-/γ-MnO_2-N per gram basis could be directed by how many moles of Mn^{n+} species were present in the pores with sizes of ≥2.7 (±0.2) Å (kinetic diameter of H_2O_2[27]). This was because $^{\bullet}OH \rightarrow NO_3^{\bullet}{}_{SUP}$ can be initiated by catalytic H_2O_2 cleavage on Mn^{n+} species. These suggested that $^{\bullet}OH \rightarrow NO_3^{\bullet}{}_{SUP}$ efficiencies on α-/β-/γ-MnO_2-N could be drastically affected by their textural features or diffusional artifacts originating from H_2O_2. This again justified the necessity to evaluate $^{\bullet}OH \rightarrow NO_3^{\bullet}{}_{SUP}$ efficiencies per site basis under diffusion-free environments to precisely investigate the geometrical effect of α-/β-/γ-MnO_2-N on $^{\bullet}OH \rightarrow NO_3^{\bullet}{}_{SUP}$ efficiencies. Interestingly, α-/β-/γ-MnO_2 lacked microporosities. Microporosities were anticipated to be observed across the catalysts, as conjectured based on their tunnel sizes illustrated in Figure 1D−F. These might be due in part to the hydrothermal synthetic technique utilized or structural collapse of α-/β-/γ-MnO_2 hosts upon the removal of guest synthetic solvents, as reported elsewhere.[49,50] Nonetheless, this could indicate that a significant portion of Mn^{n+}/O_α species were deposited in the pores with sizes of ≥20 Å, thereby helping improve the access of $NO_3^{\bullet}{}_{SUP}$ species on α-/β-/γ-MnO_2-N to phenol with the size of ~6.7 Å[51] or textile wastewater.

Bulk crystallographic features of α-/β-/γ-MnO_2 were explored using their XRD patterns, where the diffractions were in close alignment with those simulated for *tetragonal* α-/β-MnO_2 and *orthorhombic* γ-MnO_2 with no collateral diffractions assigned (Figure S1). The bulk structural characteristics of the catalysts were maintained in their surfaces. This was proved by the SAED patterns of the catalysts, wherein all spots were indexed to those simulated for α-/β-/γ-MnO_2 (Figure 2G−I). The morphological traits of the catalysts were then inspected using their HRTEM images, in which α-/β-/γ-MnO_2 were composed of 1−5-μm-sized chunks (Figure 2A−C) with the lattice fringes (d) of 1.4 Å, 3.1 Å, and 2.3 Å, respectively (Figure 2D−F). These were assigned to surface facets of (002) for *tetragonal* α-MnO_2, (110) for *tetragonal* β-MnO_2, and (400) for *orthorhombic* γ-MnO_2,

https://doi.org/10.1021/jacsau.1c00124
JACS Au 2021, 1, 1158−1177

respectively, all of which were also indexed in the SAED patterns of the catalysts. All the analytic results suggested that α-/β-/γ-MnO_2 were bulk/surface phase-pure, synthesized as targeted, and could be such platforms as to bear Mn^{n+}/O_α species for $^\bullet OH \rightarrow NO_3^\bullet{}_{SUP}$.

The numbers and strengths of Lewis acidic Mn^{n+} (n = 2 or 3) species (Lewis acidities) are pivotal to prompt $^\bullet OH$ production, whose rate-determining stage could be $^\bullet OH$ desorption from the Mn^{n+} species, as discussed in the Introduction. Hence, the surface traits of α-/β-/γ-MnO_2 were investigated using the XPS technique. Their XP spectra exhibited two broad bands in the Mn $2p_{3/2}$ and Mn $2p_{1/2}$ domains. The bands stated above were deconvoluted to provide three sub-bands with binding energies centered at ∼640.3 eV, ∼641.3 eV, and ∼642.3 eV in the Mn $2p_{3/2}$ domains, each of which could be assigned to Mn^{2+}, Mn^{3+}, and Mn^{4+} species with the separation of 12.0 eV from those present in the Mn $2p_{1/2}$ domains (Figure S2).[52] Again, Mn^{n+} species adjacent to oxygen vacancies were defective and thus can bind with H_2O_2,[35] as discussed earlier. However, the relative abundances of surface Mn^{n+} species were similar across the catalysts (20.3−25.2% in Figure 2J). In addition, CO is comparable to H_2O_2 in size (3.2 Å),[53] can bind with Lewis acidic species only, and therefore served as a probe to quantify the amounts of Lewis acidic sites included in a gram of α-/β-/γ-MnO_2 (N_{CO}) via the CO-pulsed chemisorption technique at 40 °C (near ambient temperature).[26−28] The N_{CO} values of the catalysts stayed under similar magnitudes (∼0.5 μmol_{CO} g_{CAT}^{-1} in Figure 2J) and were in good agreement with their surface Mn^{n+} concentrations. The relative abundance of surface Mn^{n+} defects innate to the catalysts was further inspected using their Raman spectra, by which oxygen vacancies vicinal to Mn^{n+} species were quantifiable using the locations/intensities of the bands centered at Raman shifts of 628.7−630.2 cm^{-1} (Figure S3). These bands could result from symmetric stretching vibrations of Mn−O bonds innate to *octahedral* $[Mn^{4+}\text{-}(O^{2-})_6]^{8-}$ subunits for α-/β-/γ-MnO_2 architectures.[54,55] These bands, however, were alike in terms of their locations and intensities, which suggested similar concentrations of oxygen vacancies (Mn^{n+} species) across the catalysts.[54,55] The EPR spectra of the catalysts were also collected at −223 °C for quantifying the concentrations of oxygen vacancies included in the catalysts with improved amplitude and resolution. The resulting EPR spectra revealed symmetric signals with g-factor values of 2.004−2.007 (Figure S4), which could originate from free electrons trapped in paramagnetic oxygen vacancies adjacent to Mn^{n+} species inherent to the catalysts.[52,56] Interestingly, the EPR signal of γ-MnO_2 was broader than those of α-/β-MnO_2 (Figure S4), which was caused by the transition of magnetic properties for γ-MnO_2 from paramagnetism to antiferromagnetism at ≤ −181 °C.[57] Nonetheless, the areas under the EPR signals of α-/β-MnO_2 were comparable and thus further corroborated the similar concentrations of oxygen vacancies included in α-/β-MnO_2.[52,56] Apparently, the XP/Raman/EPR spectra of the catalysts provide evidence that the geometrical difference among α-/β-/γ-MnO_2 could hardly diversify the quantities of Lewis acidic Mn^{n+} species included per gram of the catalysts.

However, this provided an impetus to explore H_2O_2 scission efficiencies per site basis, whose $^\bullet OH$ productivities could be mainly dictated by the Lewis acidic strengths of surface Mn^{n+} sites. In this regard, XP spectra of α-/β-/γ-MnO_2 in the Mn 3s regimes were explored (Figure S2). The XP spectra were deconvoluted to provide two sub-bands,[39,58] whose peak splitting ($\Delta E_{BINDING\ ENERGY}$) was 4.50, 4.48, or 4.55 eV for α-, β-, or γ-MnO_2. The $\Delta E_{BINDING\ ENERGY}$ values could be converted to the average oxidation state (AOS) of surface Mn species using the relationship of AOS = 8.956−1.126 × $\Delta E_{BINDING\ ENERGY}$.[39,58] The AOS values of α-/β-/γ-MnO_2 were ≥3.8, which was expected given the surface concentrations of Mn^{4+} species (≥∼75.0%) for the catalysts. However, the AOS of γ-MnO_2 (3.83) was smaller than those of α-/β-MnO_2 (∼3.90), which could suggest the smallest Lewis acidic strength of Mn^{n+} species inherent to γ-MnO_2 (Figure 2K). In addition to the similarity found in H_2O_2, CO, and CO_2 molecules (3.3 Å)[59] in sizes, the lone pair of e^- present in CO_2 can be coordinated to Lewis acidic metals[28,60] and thus served as an additional probe to quantify the Lewis acidic strengths of Mn^{n+} species inherent to the surfaces. For this purpose, the CO_2 isotherms of the catalysts were collected at −20 °C∼20 °C (near ambient temperature) and subjected to Toth fittings in order to extract isosteric heats of CO_2 adsorption for the catalysts ($-Q_{ST,CO2}$) at a near-zero coverage of CO_2 with the use of the Clausius−Clapeyron equation (Figure S5).[61,62] Interestingly, $-Q_{ST,CO2}$ of β-MnO_2 was ∼5.0 kJ mol_{CO2}^{-1} (Figure 2K). This might be ascribed to the low porosity of β-MnO_2 (∼10 m^2 g_{CAT}^{-1}) amicable to enhance lateral $CO_2\cdots CO_2$ interactions rather than $CO_2\cdots Mn^{n+}$ interactions[60,63] and therefore remained challenging to accurately quantify $CO_2\cdots Mn^{n+}$ interactions via $-Q_{ST,CO2}$. However, $-Q_{ST,CO2}$ of γ-MnO_2 (∼42.9 kJ mol_{CO2}^{-1}) was smaller than that of α-MnO_2 (∼51.1 kJ mol_{CO2}^{-1}). In conjunction with the AOS values, the $-Q_{ST,CO2}$ values highly suggested that Lewis acidic Mn^{n+} species could be most desired in expediting $^\bullet OH$ desorption, when being deposited on a γ-MnO_2 surface. Noteworthily, the lone e^- pair innate to CO_2 can also bind with the proton of surface Brönsted acidic sites (−OH), as reported previously.[64,65] Indeed, α-/β-/γ-MnO_2 surfaces afforded Brönsted acidic (***B***) and Lewis acidic (***L***) sites, as supported by their background-subtracted, *in situ* DRIFT spectra. As shown in Figure S6, ***B***/***L*** bands resulting from asymmetric or symmetric stretching (or bending) vibrations of N−H bonds of NH_3 coordinated to ***B***/***L*** sites were developed under a NH_3 atmosphere at 50 °C (near ambient temperature).[18,39,66−68] Nevertheless, the areas under the ***L*** bands were greater than those of the ***B*** bands across the catalysts. This could indicate that the $-Q_{ST,CO2}$ values of the catalysts mainly originated from $CO_2\cdots Mn^{n+}$ interactions, although the contributions of $CO_2\cdots$***B*** interactions to the $-Q_{ST,CO}$ values could not be ruled out entirely. Nevertheless, AOS and $-Q_{ST,CO2}$ analysis on α-/β-/γ-MnO_2 could aid in establishing the hierarchy with regard to the Lewis acidic strengths of Mn^{n+} species adequate to desorb $^\bullet OH$ in the following order of α-MnO_2 ∼ β-MnO_2 < γ-MnO_2.

On the other hand, the surface area of Lewis acidic Mn^{n+} species (S_{CO}) can be closely related to the frequency of $H_2O_2\cdots Mn^{n+}$ collisions, thereby directing the prefactor ($k_{APP,0}$) of the catalyst in H_2O_2 scission or the $^\bullet OH$-mediated pollutant degradation run, as we suggested earlier.[28,39] Hence, the S_{CO} ($S_{BET,CO}$ divided by N_{CO}) values of the catalysts were quantified with the use of their CO isotherms, all of which provided CO-accessible BET surface areas ($S_{BET,CO}$) along with the amounts of CO adsorbed per gram of the catalysts at 1 bar (N_{CO}).[28,39] It should be noted that CO_2 isotherm experiments could also provide S_{CO2} values of the catalysts analogous to their S_{CO} counterparts yet were not considered due to CO_2 adsorption on Brönsted acidic sites (Figure S5).

https://doi.org/10.1021/jacsau.1c00124
JACS Au 2021, 1, 1158−1177

We attempted to collect CO isotherms of the catalysts near ambient temperature. However, the CO isotherms revealed minute differences in terms of $S_{BET,CO}$ and N_{CO} values throughout the catalysts at ≥ −20 °C due to the limitation of the instrument used[28] (not shown) and therefore were collected at −30 °C only (Figure S7). The S_{CO} values of the catalysts increased in the following order of γ-MnO_2 (~3.0 × 10^5 m_{CO}^2 mol_{CO}^{-1}) < α-MnO_2 (~3.9 × 10^5 m_{CO}^2 mol_{CO}^{-1}) < β-MnO_2 (~6.6 × 10^5 m_{CO}^2 mol_{CO}^{-1}). This suggested β-MnO_2 might be most desired in producing •OH among the catalysts, in spite of its greatest intimacy with •OH (evidenced by AOS analysis).

H_2O_2 Scission Kinetics on α-/β-/γ-MnO_2

H_2O_2 scission/pollutant degradation runs on the catalysts were then conducted at 25 °C, whose details are given in the Supporting Information and figure captions. Of note, it was reported that H_2O_2 can be dissected on surface-unbound Mn^{2+} and Mn^{3+} to produce •OH and regenerate Mn^{2+} with moderate k values of ~1.3 × 10^1 M^{-1} s^{-1} and ~2.8 × 10^3 M^{-1} s^{-1}, respectively.[29,30] Of note, in spite of having a longer life span ($t_{1/2}$ of 2.0 × 10^6 μs), •OOH possesses smaller electrophilicity (E_0 of 1.8 V) than that of •OH.[29,30,69] •OOH thus might not likely serve to fragment contaminant (Figure 1A). Of additional note, •OOH can be also cleaved to form $O_2^{\bullet-}$ with the smallest electrophilicity among the radicals considered (E_0 of −0.2 V).[29,30,70] Given the reaction of Mn^{3+} (surface-unbound) + $O_2^{\bullet-}$ → Mn^{2+} (surface-unbound) + O_2 with a large k of ~7.0 × 10^7 M^{-1} s^{-1},[30] $O_2^{\bullet-}$ might be utilized to recover surface Mn^{n+} species, as illustrated in Figure 1A. The potential functions of •OH/H_2O_2/•OOH/$O_2^{\bullet-}$ depicted above could suggest their vitality in decomposing pollutant (via •OH) and/or regenerating surface Mn^{n+} species (via H_2O_2 or •OOH/$O_2^{\bullet-}$). This thus rationalized the use of an excess amount of H_2O_2 (30 mmol) relative to that of Mn^{n+} species inherent to the catalyst (~0.5 μmol_{CO} g_{CAT}^{-1}) throughout the reaction runs.

Of additional note, H_2O_2 can experience self-decomposition under aqueous environments to evolve •OOH/$O_2^{\bullet-}$ even in the absence of the catalysts[26−28,71] and therefore should be regarded as background. Thus, reaction data were corrected using backgrounds and fitted via a pseudo-first-order kinetic model (Figure S8) to extract apparent reaction rate constants of the catalysts (k_{APP}).[26−28] Moreover, the change in type of MnO_2 polymorphs did not alter their N_{CO} values yet did vary their $-Q_{ST,CO2}$ values along with the AOS values of surface Mn species. This indicated that H_2O_2 scission efficiencies on the catalysts could rely mainly on the Lewis acidic strengths of Mn^{n+} species. Therefore, the initial H_2O_2 scission rates of the catalysts were evaluated via the site basis and defined as the amounts of H_2O_2 cleaved per CO-accessible Lewis acidic site per unit time ($-r_{H2O2,0}$ in eq S4).[26−28] The $-r_{H2O2,0}$ values of α-/β-MnO_2 were comparable (~25 min^{-1}) yet were smaller than that of γ-MnO_2 (~35 min^{-1} in Figure 3A), which indicated that Mn^{n+} species innate to γ-MnO_2 possessed Lewis acidic strength most desirable to generate •OH/•OOH/$O_2^{\bullet-}$. The trend found in the $-r_{H2O2,0}$ values of α-/β-/γ-MnO_2 was in exact and partial alignments with those found in the AOS values of surface Mn species and the $-Q_{ST,CO2}$ values of the catalysts, respectively. All the results were gathered to demonstrate that Mn^{n+} species with smaller Lewis acidic strengths could accelerate •OH desorption (rate-determining step) more efficiently and thus resulted in a higher $-r_{H2O2,0}$ of

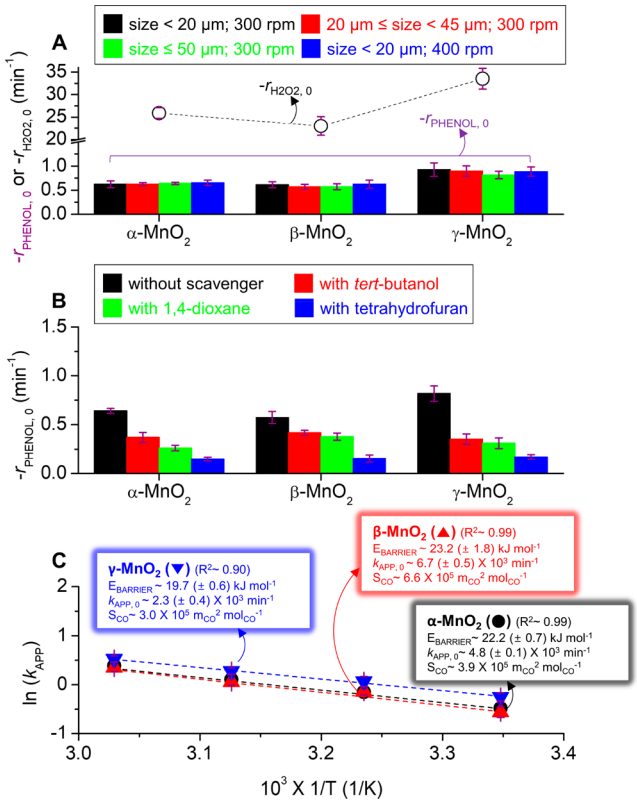

Figure 3. (A) Background-subtracted initial H_2O_2 scission rates ($-r_{H2O2,0}$) and initial phenol decomposition rates ($-r_{PHENOL,0}$) of α-, β-, or γ-MnO_2, for which particle size or stirring speed was varied during phenol decomposition runs. (B) Change in $-r_{PHENOL,0}$ values for α-, β-, or γ-MnO_2 in the absence or the presence of quencher (*tert*-butanol, 1,4-dioxane, or tetrahydrofuran). (C) Arrhenius plots ($\ln(k_{APP})$ versus $10^3/T$) for α-, β-, or γ-MnO_2, whose apparent reaction rate constants (k_{APP}) were obtained from phenol decomposition runs at 25∼55 °C. Reaction conditions: 0.2 g of the catalysts with the sizes of ≤50 μm (H_2O_2 scission A, B, and C) or <20 μm/20−45 μm/≤50 μm (phenol decomposition A); 100 mL of deionized H_2O; 30 mmol of H_2O_2; 0 mmol (H_2O_2 scission A) or 0.1 mmol of phenol (phenol decompositions A, B, and C); 0 mmol of A and C or 60 mmol of quencher B; pH of 7.0; 25 °C (A and B) or 25∼55 °C (C); 300 rpm (H_2O_2 scission (A, B, and C) or 400 rpm (phenol decomposition (A)).

the catalyst, as also proven in our previous studies on the •OH → $SO_4^{\bullet-}{}_{SUP}$ route for NiO and Fe-modified Mn_3O_4.[27,28]

The evolution of •OH/•OOH/$O_2^{\bullet-}$ during catalytic H_2O_2 dissection on α-/β-/γ-MnO_2 was apparent. This was evidenced by EPR spectra of reaction mixtures and solutions collected upon the filtration of reaction mixtures, whose compositions were identical to those used to perform H_2O_2 scission runs except for adding DMPO as a spin trapper of •OH/•OOH/$O_2^{\bullet-}$. It was reported that DMPO can be rapidly coordinated to •OH or •OOH for its transition to DMPO-OH or DMPO-OOH adducts (Figures 4A and S9), whose lifetimes are sufficiently long enough to be detected and thus qualitative in EPR spectroscopy experiments.[72,73] Interestingly, DMPO can also bind with $O_2^{\bullet-}$ to produce DMPO-O_2 intermediate, which in turn interacts with H^+ under aqueous medium to finally transform into DMPO-OOH adduct, as reported elsewhere.[74] Indeed, the EPR spectra revealed large quartet signals with hyperfine splitting constants of 14.8 G for a(^{14}N)/a(^{1}H) and intensity ratios of 1:2:2:1,[72,73] which typically indicated the

https://doi.org/10.1021/jacsau.1c00124
JACS Au 2021, 1, 1158−1177

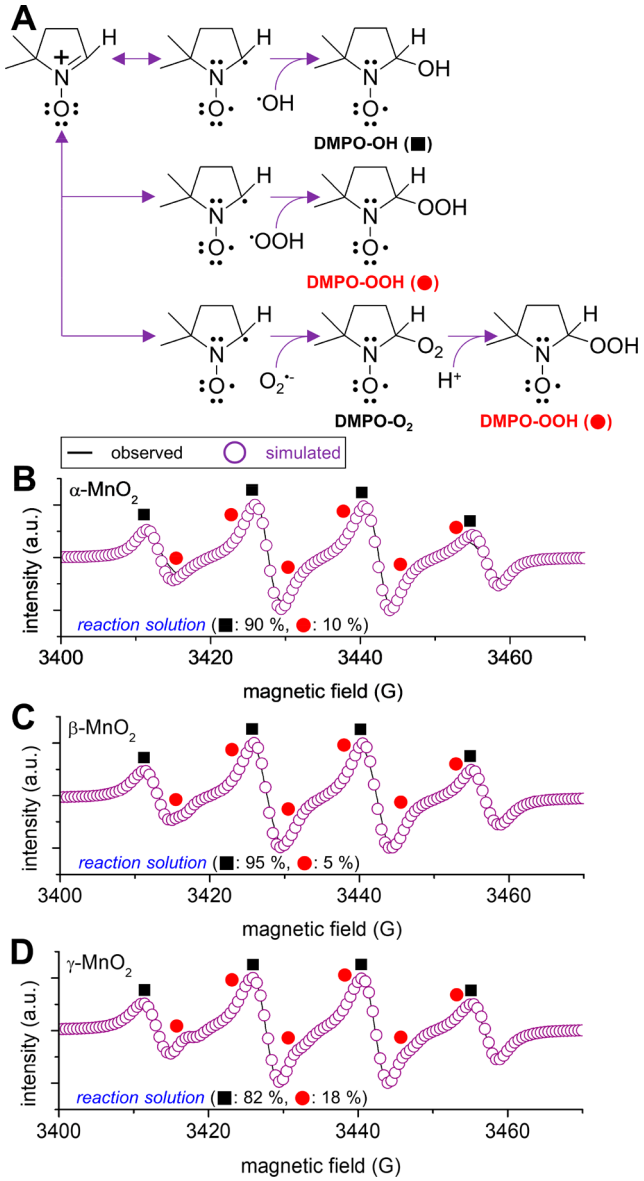

Figure 4. (A) Formation mechanisms of DMPO-OH and DMPO-OOH adducts. EPR spectra of reaction aliquots (liquid) taken from reaction mixtures (solid (catalyst) + liquid) that underwent filtration using a 0.45-μm-sized PES syringe (B–D). Reaction mixtures included DMPO as a spin trapper for $^{\bullet}OH/^{\bullet}OOH/O_2^{\bullet-}$ and α-MnO_2 (B), β-MnO_2 (C), or γ-MnO_2 (D) as a catalyst. In B–D, black solid lines and empty purple circles indicate raw and simulated EPR spectra, respectively. Black solid squares and red solid circles indicate DMPO-OH and DMPO-OOH adducts, respectively, whose relative abundance was simulated and exhibited in parts B–D. Reaction mixture: 2 mg of the catalyst with the sizes of $\leq$50 μm; 1 mL of deionized H_2O; 0.3 mmol of H_2O_2; 3 mmol of DMPO; pH of 7.0; 25 °C; vortex for 2 min.

presence of DMPO-OH (black squares in Figures 4B–D and S9). In addition, the EPR spectra also exhibited sextet signals with hyperfine splitting constants of 14.4 and 11.2 G for a(^{14}N) and a(^{1}H), respectively,[72,73] which could demonstrate the presence of DMPO-OOH (red circles in Figures 4B–D and S9). Of importance, ERP spectroscopy experiments were reported of particular challenge to precisely quantify multiple paramagnetic adducts due to overlap and/or broadness of their spectral signals.[75−77] Hence, although the relative abundance of DMPO-OH (80–95%) and DMPO-OOH (5–20%) is quantifiable upon the simulation of the EPR spectra, it should be utilized only for rough comparison. Of additional importance, the EPR spectra observed and simulated did show good agreement post the inclusion of DMPO-OOH species in the simulated EPR spectra, albeit with their small relative abundance. This suggested that the evolution of $^{\bullet}OOH$ might be as phenomenal as that of $^{\bullet}OH$ during catalytic H_2O_2 scission. Interestingly, in spite of the challenge associated with the accurate quantification of the adducts, the EPR spectra of reaction mixtures (solid (catalyst) + liquid; Figure S9) were comparable to those of reaction solutions (liquid; Figure 4B–D). This could indicate that $^{\bullet}OH/^{\bullet}OOH/O_2^{\bullet-}$ species were mostly present in reaction solutions and thereby demonstrated the liberation of $^{\bullet}OH/^{\bullet}OOH/O_2^{\bullet-}$ species from the catalyst surfaces to liquid phases, as depicted in Figure 1A.

Meanwhile, phenol is one of the aromatics with −OH functionality, both of which are particularly arduous to be fragmented under aqueous medium.[26−28] Therefore, phenol was utilized as a model compound of aqueous contaminants. Phenol decomposition runs on the catalysts were conducted under identical conditions to those utilized to perform H_2O_2 scission runs except for adding 0.1 mmol of phenol to reaction mixtures. It should be stressed that phenol adsorption on α-/β-/γ-MnO_2 surfaces was not trivial and was as considerable as phenol degradation mediated by $^{\bullet}OH/^{\bullet}OOH/O_2^{\bullet-}$ evolved via H_2O_2 self-decomposition (not shown). Hence, phenol adsorption on the catalyst surfaces was also deemed as background utilized for correcting reaction data (Figure S10). This could provide the initial phenol decomposition rates of the catalysts ($-r_{PHENOL,0}$ in eq S6), whose definition was analogous to that of $-r_{H2O2,0}$.[26−28]

It should also be emphasized that to rigorously assess the $-r_{PHENOL,0}$ values (activities) of the catalysts, it is imperative to ensure the $-r_{PHENOL,0}$ values are evaluated under reaction-limited regimes, in which the $-r_{PHENOL,0}$ values are not affected or directed by diffusional artifacts[78,79] such as the transport of phenol (or $^{\bullet}OH$) from the aqueous phase to $NO_3^{\bullet}$ (or NO_3^-) grafted on the exterior surfaces of the catalysts (denoted as external diffusion) and the transport of phenol (or $^{\bullet}OH$) from the exterior surfaces of the catalysts to $NO_3^{\bullet}$ (or NO_3^-) anchored inside the catalyst pores (denoted as inter(or intra)particle diffusion; internal diffusion).[27] In this regard, SEM analysis of the catalysts was performed to evaluate their particle sizes, most of which were $\leq$50 μm (Figure S11). Hence, the catalysts were sieved to vary their particle sizes of <20 μm, 20–45 μm, or $\leq$50 μm and subjected to phenol degradation runs to inspect the significance of internal diffusional artifacts on the $-r_{PHENOL,0}$ values.[27] In addition, the stirring speed of the reaction mixtures during phenol degradation runs was also altered to investigate the significance of external diffusional artifacts on the $-r_{PHENOL,0}$ values (300 or 400 rpm).[27] The resulting $-r_{PHENOL,0}$ values of the catalysts, however, were invariant even with the alteration of the reaction conditions mentioned above (catalyst particle sizes or stirring speeds). This could provide evidence that $-r_{PHENOL,0}$ values were evaluated under diffusion-free environments. In addition, the $-r_{PHENOL,0}$ values of the catalysts were smaller than those of the corresponding $-r_{H2O2,0}$ counterparts, which was due possibly to the short lifetime of $^{\bullet}OH$ or $O_2^{\bullet-}$ (Figure 3A). Nonetheless, the trends found in $-r_{H2O2,0}$ and $-r_{PHENOL,0}$ values for the catalysts were identical (i.e., $-r_{PHENOL,0}$ of ~0.6 min^{-1} for α-/β-MnO_2; ~0.8 min^{-1} for γ-MnO_2).

https://doi.org/10.1021/jacsau.1c00124
JACS Au 2021, 1, 1158−1177

Moreover, γ-MnO_2 leached a moderate amount of Mn species after 8 h of phenol decomposition runs (~2.5 mol % for α-MnO_2; ~0.1 mol % for β-MnO_2; ~0.5 mol % for γ-MnO_2). All of the results helped suggest that Mn^{n+} species innate to γ-MnO_2 could desorb $^{\bullet}OH$ most proficiently.

Our claim stated above could be partially convincing, unless the solid proof on the role of $^{\bullet}OH$ as the main degradation product of phenol was presented. In this regard, a series of scavengers with distinct secondary rate constants in quenching $^{\bullet}OH$ ($k_{\bullet OH}$) were selected such as *tert*-butanol (~6.0×10^8 M^{-1} s^{-1}), 1,4-dioxane (~3.1×10^9 M^{-1} s^{-1}), and tetrahydrofuran (~4.0×10^9 M^{-1} s^{-1}), whose specifics are also given in Table S6 with references cited. The conditions utilized for scavenging runs were identical to those used to perform phenol decomposition runs, except for adding scavengers, whose quantities were twice that of H_2O_2 utilized (Figure S12).[26−28] It was expected that $-r_{PHENOL,0}$ of a catalyst decreased upon the addition of a scavenger. However, $-r_{PHENOL,0}$ should be higher in the presence of a scavenger with a smaller $k_{\bullet OH}$, if the phenol degradation were primarily directed by $^{\bullet}OH$. The reduction of $-r_{PHENOL,0}$ values for α-/β-/γ-MnO_2 was more pronounced in the following order of "with *tert*-butanol → with 1,4-dioxane → with tetrahydrofuran", which was concurrent to the hierarchy on the $k_{\bullet OH}$ values for the scavengers (Figure 3B). This suggested that $^{\bullet}OH$ could function as the main degrader of phenol upon H_2O_2 splitting on α-/β-/γ-MnO_2 surfaces. In addition, *tert*-butanol was reported to barely quench $^{\bullet}OOH$ ($k_{\bullet OOH}$ of ~7.1×10^1 M^{-1} s^{-1}) or $O_2^{\bullet-}$ and thereby should not decline $-r_{PHENOL,0}$ of a catalyst if $^{\bullet}OOH$ or $O_2^{\bullet-}$ acted as a major decomposer of phenol. However, the reduction of $-r_{PHENOL,0}$ values was substantial across the catalysts in the presence of *tert*-butanol, which could corroborate that $^{\bullet}OOH$ or $O_2^{\bullet-}$ was hardly exploited to decompose phenol with α-/β-/γ-MnO_2 in use as catalysts. In addition to the nature of $O_2^{\bullet-}$ almost inactive in decomposing phenol,[80] scavenging runs could provide concrete evidence that $^{\bullet}OH$ was deployed to fragment phenol. In addition to the EPR spectra of the catalysts validating the evolution of $^{\bullet}OOH$ and/or $O_2^{\bullet-}$ during H_2O_2 scission runs (Figures 4 and S9), scavenging runs validated that $^{\bullet}OOH$ and/or $O_2^{\bullet-}$ were the major species acting as a reductant of $M^{(\delta+1)+}$ for the recovery of $M^{\delta+}$.

Additional control runs were performed to inspect if Mn^{n+} species could produce $^{\bullet}OH$ via heterogeneous catalytic scission of H_2O_2. The reaction conditions were identical to those utilized to perform phenol decomposition runs except for vacuum filtration of reaction mixtures to collect reaction solutions after an hour of reaction runs. Phenol conversions (X_{PHENOL}) of the resulting reaction solutions then kept being monitored up to 8 h of reaction runs (denoted as the filtration run in Figure S13).[26−28] In addition, the H_2O_2 self-decomposition run in the absence of the catalyst was conducted and monitored with regard to X_{PHENOL} values up to 8 h, for comparison. The H_2O_2 self-decomposition run showed the increase in X_{PHENOL} values of 4.3 (±0.5)% at 1−8 h ($\Delta X_{PHENOL,BLANK}$), which could be attributed to $^{\bullet}OOH$ or $O_2^{\bullet-}$ indispensably evolved, as reported previously.[26−28,71] Interestingly, $\Delta X_{PHENOL,BLANK}$ obtained during the H_2O_2 self-decomposition run was in similar magnitude to ΔX_{PHENOL} values obtained during filtration runs at 1−8 h (5.2 (±0.8)% for α-MnO_2; 4.3 (±0.4)% for β-MnO_2; 4.7 (±1.2)% for γ-MnO_2). This clearly indicated that unsupported, leached Mn^{n+} species tentatively present in reaction solutions did play a marginal role in producing $^{\bullet}OH$ used to decompose phenol. Filtration runs validated that α-/β-/γ-MnO_2 could degrade phenol with the main use of $^{\bullet}OH$ species generated via heterogeneous catalytic H_2O_2 scission on surface Mn^{n+} species.

Again, $-r_{H2O2,0}/-r_{PHENOL,0}$ values of α-/β-/γ-MnO_2 could increase at a higher temperature (Figure S14). This was because a larger heat energy was delivered to the catalyst surface and helped overcoming the energy barrier ($E_{BARRIER}$) required to desorb $^{\bullet}OH$ from surface Mn^{n+} species at a greater temperature.[26−28] This indicated that the reactions should conform to the Arrhenius behavior.[26−28] Hence, additional control runs were performed identically to phenol decomposition runs except for altering the temperatures from 25 to 55 °C, at which the k_{APP} values of the catalysts were obtained. The resulting k_{APP} values served to establish Arrhenius plots of $\ln(k_{APP})$ versus $1/T$ for the catalysts, whose slopes and y-intercepts were used to extract the kinetic parameters of $E_{BARRIER}$ values and prefactors ($k_{APP,0}$), respectively (Figure 3C).[26−28] The $E_{BARRIER}$ values of the catalysts increased in the following order: γ-MnO_2 (~19.7 kJ mol^{-1}) < α-MnO_2 ~ β-MnO_2 (~22.7 kJ mol^{-1}). This was in close line with the hierarchy of Lewis acidic strengths identified via AOS of Mn species and $-Q_{ST,CO2}$ values for the catalysts (Figure 2K). This again demonstrated that $^{\bullet}OH$ desorption could dominate the H_2O_2 scission cycle on α-/β-/γ-MnO_2. In addition, the $k_{APP,0}$ values of the catalysts increased in the following sequence of γ-MnO_2 (~2.3×10^3 min^{-1}) < α-MnO_2 (~4.8×10^3 min^{-1}) < β-MnO_2 (~6.7×10^3 min^{-1}), which was in exact agreement with the hierarchy found in their S_{CO} values, as discussed above. This also indicated that the β-MnO_2 surface provided the greatest probability for H_2O_2 to collide with Mn^{n+} per unit time. Nonetheless, γ-MnO_2 showed the greatest $-r_{PHENOL,0}$ values throughout all temperatures considered, which clarified that the small Lewis acidic strength of the Mn^{n+} species was pivotal to achieve high $^{\bullet}OH$ productivity on α-/β-/γ-MnO_2 surfaces via H_2O_2 scission.

Properties of α-/γ-MnO_2-N

α-/β-/γ-MnO_2 were subjected to NO_Y^- functionalization to form α-/β-/γ-MnO_2-N upon their exposure to the NO/O_2 stream for an hour, for which the NO concentration and temperature were adjusted to 5,000 ppm and 150 °C through the optimization for achieving the greatest quantities of N species deposited on the resulting α-/γ-MnO_2-N surfaces. (Details are given in the Supporting Information.) Interestingly, the β-MnO_2 surface was attempted to be modified with NO_Y^- species under a variety of conditions yet could not afford NO_Y^- functionalities. Again, this could be due in part to the small porosity of β-MnO_2, by which Mn^{n+} and O_α species were in limited access to NO_Y^- and NO/O_2 even under an optimized environment used to settle down NO_Y^- functionalities in α-/γ-MnO_2 surfaces. The properties of α-/γ-MnO_2-N were characterized using a host of techniques and compared with those of α-/γ-MnO_2. The crystallographic and morphological traits of α-/γ-MnO_2 were unchanged post their modification with NO_Y^- species. This was evidenced by XRD patterns (Figure S1), SAED patterns (Figure S15E−S15F), and lattice fringes (d) in HRTEM images (Figure S15A−S15D) of α-/γ-MnO_2-N, whose details are illustrated in the figure captions. Conversely, the S_{BET} and V_{BJH} values of α-/γ-MnO_2-N were smaller than those of α-/γ-MnO_2 by 10−20 m^2 g_{CAT}^{-1} and ~0.1 cm^3 g_{CAT}^{-1}, as clarified by N_2 isotherm

https://doi.org/10.1021/jacsau.1c00124
JACS Au 2021, 1, 1158−1177

experiments. This could be ascribed to the occupation of NO_Y^- functionalities inside the pores of α-/γ-MnO_2-N.

In addition, the amounts of Lewis acidic sites present in α-/γ-MnO_2 decreased post NO_Y^- functionalization. This was corroborated by deconvoluted XP spectra of α-/γ-MnO_2 and α-/γ-MnO_2-N in the Mn 2p domains,[52] where the relative abundance of Mn^{n+} species was reduced from 25.2% to 18.0% for α-MnO_2 and from 20.3% to 16.5% for γ-MnO_2 post the modification with NO_Y^- functionalities (Figures 5A and S2).

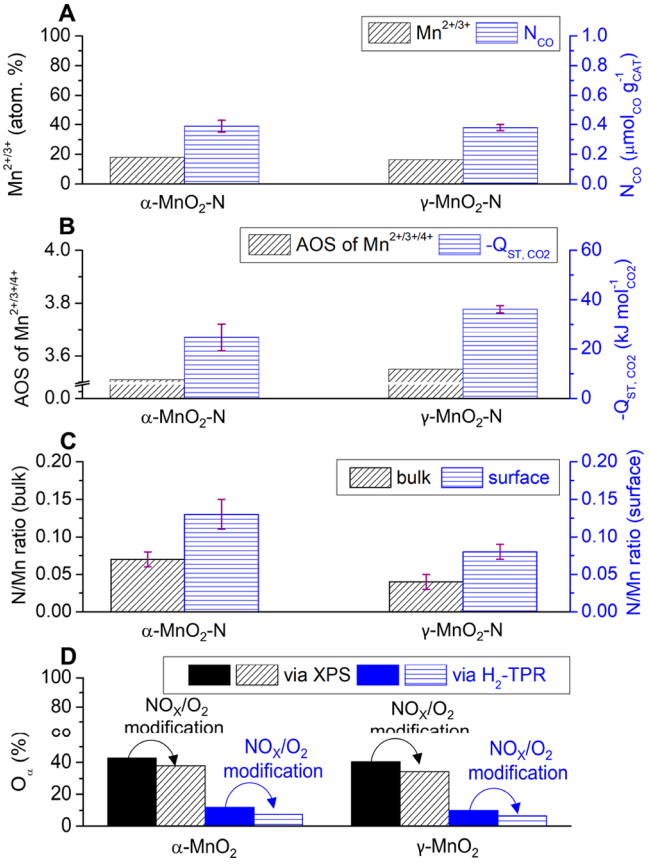

Figure 5. (A) Atomic concentrations of Mn^{2+}/Mn^{3+} species present in or near the surfaces of α-MnO_2-N and γ-MnO_2-N and their N_{CO} values. (B) AOS values of $Mn^{2+}/Mn^{3+}/Mn^{4+}$ species present in or near the surfaces of α-MnO_2-N and γ-MnO_2-N and their $-Q_{ST,\,CO2}$ values with small CO_2 coverages (~5.1 μmol g_{CAT}^{-1} for α-MnO_2-N and γ-MnO_2-N). (C) Molar ratios of N to Mn (N/Mn) innate to α-MnO_2-N and γ-MnO_2-N analyzed via XRF/EA (for bulk) and XP spectroscopy (XPS; for surface). (D) Relative abundance of labile O species (O_α) inherent to α-MnO_2, α-MnO_2-N, γ-MnO_2, and γ-MnO_2-N analyzed via XPS and H_2-TPR.

This was in close agreement with CO-pulsed chemisorption analysis of the catalysts,[26−28] wherein N_{CO} values also declined from ~0.5 μmol_{CO} g_{CAT}^{-1} to ~0.4 μmol_{CO} g_{CAT}^{-1} for α-/γ-MnO_2 after NO_Y^- functionalization (Figure 5A). Raman spectra of α-/γ-MnO_2-N also revealed the bands with Raman shifts centered at 631.5 and 632.0 cm^{-1}, respectively (Figure S3), whose intensities were similar to those of α-/γ-MnO_2, whereas the locations were blue-shifted relative to those of α-/γ-MnO_2 (628.7 cm^{-1} for α-MnO_2; 630.2 cm^{-1} for γ-MnO_2). This could indicate the reduction of oxygen vacancies upon the functionalization of α-/γ-MnO_2 with NO_Y^- species, leading to enhanced symmetric stretching vibrations of the Mn−O bonds of $[Mn^{4+}\text{-}(O^{2-})_6]^{8-}$ subunits for α-/γ-MnO_2-N architectures.[54,55] Moreover, this was in close alignment with the EPR spectra of α-/γ-MnO_2-N collected at −223 °C (Figure S4), in which g-factor values were almost unchanged even post NO_Y^- functionalization (2.004). The areas under the EPR signals for α-/γ-MnO_2-N were reduced markedly in comparison with those of α-/γ-MnO_2, which resulted from the decrease in the concentrations of oxygen vacancies innate to α-/γ-MnO_2 architectures modified with NO_Y^- species.[52,56] All of the analytic results stated above could corroborate that in addition to O_α species allowing for an access to NO/O_2, Mn^{n+} species on α-/γ-MnO_2 could also be grafted by gaseous NO_Y^- species that were formed in proximity to Mn^{n+} sites during the synthesis of α-/γ-MnO_2-N, which was also suggested and computed elsewhere.[36−39] Of importance, the amounts of Lewis acidic sites were comparable across the catalysts subjected to NO_Y^- modification, which again posed the need to compare $-r_{H2O2,0}/-r_{PHENOL,0}$ values of α-/γ-MnO_2-N per site basis for clarifying their geometrical effect on the $^\bullet OH \rightarrow NO_3^\bullet{}_{SUP}$ route.

Furthermore, the Lewis acidic strengths of Mn^{n+} species inherent to α-/γ-MnO_2 were also altered in such a way as to improve $^\bullet OH$ desorption from Mn^{n+} species upon NO_Y^- modification. This was substantiated by the XP spectra of the catalysts in the Mn 3s domains,[39,58] in which the $\Delta E_{BINDING\ ENERGY}$ values of α- and γ-MnO_2 increased by ~0.35 eV and ~0.25 eV post NO_Y^- functionalization (Figure S2). This led to the decrease in the resulting AOS values of surface Mn species of 3.89 for α-MnO_2 → 3.51 for α-MnO_2-N and 3.83 for γ-MnO_2 → 3.55 for γ-MnO_2-N (Figure 5B). This was also in close line with the $-Q_{ST,CO2}$ values of the catalysts obtained via CO_2 isotherm experiments (Figure S5).[61,62] Interestingly, α-MnO_2 showed a greater decrease in $-Q_{ST,CO2}$ from ~51.1 kJ mol_{CO2}^{-1} to ~24.7 kJ mol_{CO2}^{-1} at a near-zero coverage of CO_2 post NO_Y^- modification in comparison with that of γ-MnO_2 (~42.9 kJ mol_{CO2}^{-1} for γ-MnO_2; ~36.2 kJ mol_{CO2}^{-1} for γ-MnO_2-N), as depicted in Figure 5B. The analytic results on Lewis acidic strengths for the catalysts highly suggested that α-MnO_2-N could outperform γ-MnO_2-N in cleaving H_2O_2 (or producing $^\bullet OH$), thus degrading phenol better than γ-MnO_2-N based on a higher efficiency to produce $NO_3^\bullet{}_{SUP}$ species.

It should be stressed that the N_{CO} values of α-/γ-MnO_2 (~0.5 μmol_{CO} g_{CAT}^{-1}) were reduced to show ~0.4 μmol_{CO} g_{CAT}^{-1} upon NO_Y^- modification. This again could suggest that the NO_Y^- functionalities were anchored on α-/γ-MnO_2-N based on the interplays between Mn^{n+} and gaseous NO_Y^- species. Meanwhile, the formation of surface NO_Y^- species based on the interactions between NO/O_2 and O_α species was left unclarified, thus being inspected using XPS and H_2-TPR experiments. The XP spectra of the catalysts in the O 1s regimes showed a broad band, which was deconvoluted into three sub-bands assigned to lattice O (O_β), O chemically susceptible (O_α), and O of H_2O chemisorbed (O'_α) with binding energies centered at ~529.8 eV, ~530.6 eV, and ~531.9 eV, respectively (Figure S16).[28,39] β-MnO_2 with S_{BET} of ~10 m^2 g_{CAT}^{-1} provided the smallest concentration of surface O_α species (~30%) among α-/β-/γ-MnO_2. Therefore, the β-MnO_2 surface could be barely modified by NO_Y^- species and showed negligible N contents. This was evidenced by EA/XPS analytic results, all of which showed a background level of N compositions (~0) in the resulting β-MnO_2-N (not shown). We thus did not explore the properties of β-MnO_2-N. In contrast, α-/γ-MnO_2 with S_{BET} values of ≥ ~50 m^2 g_{CAT}^{-1}

https://doi.org/10.1021/jacsau.1c00124
JACS Au 2021, 1, 1158−1177

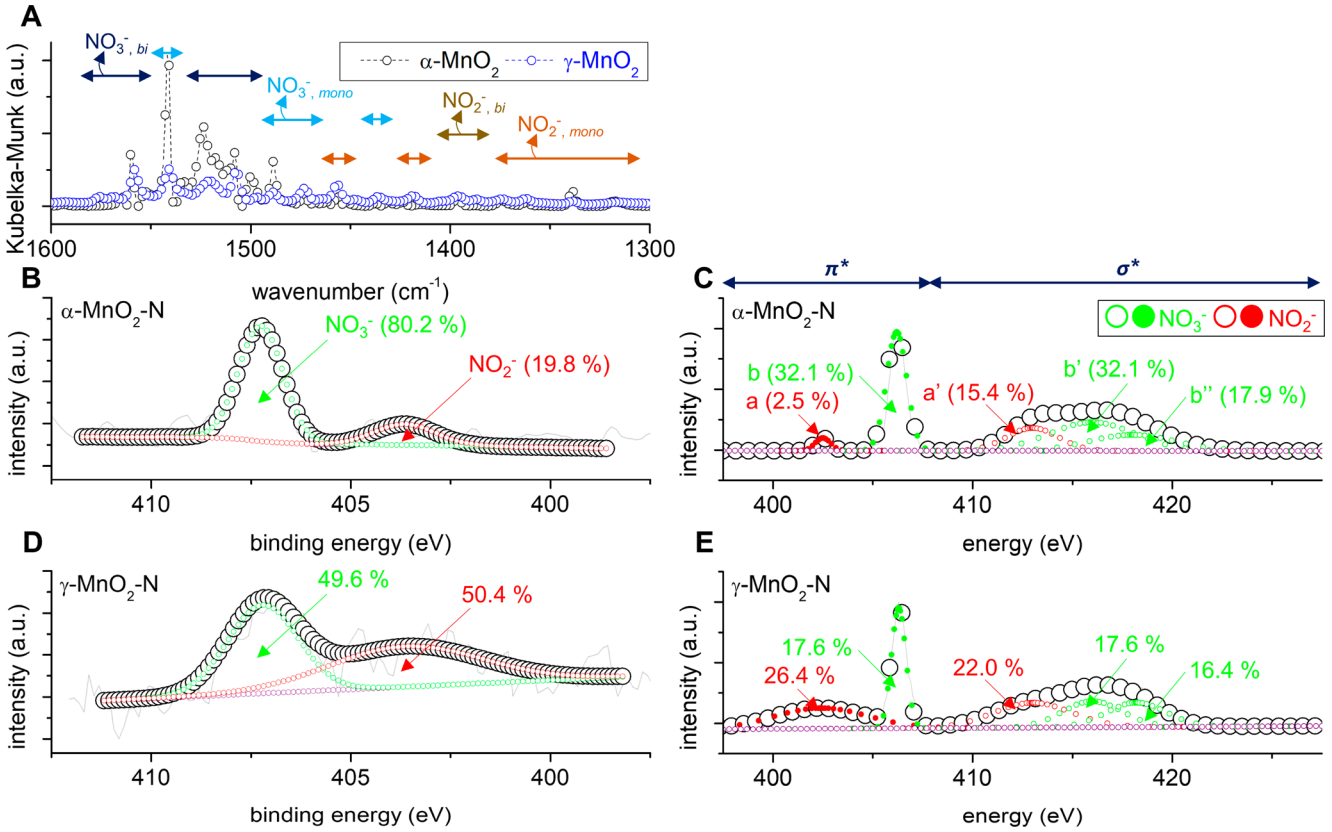

Figure 6. (A) Background-subtracted, *in situ* NO/O_2-DRIFT spectra of α-MnO_2 and γ-MnO_2 at 150 °C. The surfaces were initially purged with 3 vol % O_2/N_2 at 110 °C for an hour prior to the collection of their background signals under a N_2 at 150 °C. The spectra of the catalysts were then recorded under 1,000 ppm of NO/3 vol % O_2/N_2 at 150 °C for an hour upon the subtraction of the background signals. The ramping rate and total flow rate were 10 °C min^{-1} and 200 mL min^{-1}, respectively. In part A, NO_2^- and NO_3^- indicate vibrations of N−O bonds of NO_2^- and NO_3^- coordinated to the surface with distinct binding configuration of *mono-* (denoted as *mono*) or *bi*-dentate (denoted as *bi*). XP spectra of α-MnO_2-N (B) and γ-MnO_2-N (D) in the N 1s domains. In parts B and D, gray solid lines and black empty circles indicate raw and fitted XP spectra, respectively, whereas purple empty circles denote backgrounds. Numbers shown with arrows denote relative abundance of surface NO_2^-/NO_3^- species innate to the catalysts. XANES spectra of α-MnO_2-N (C) and γ-MnO_2-N (E) at the N K-edges, in which π^* (a and b) and σ^* resonances (a′, b′, and b′′) of surface NO_2^-/NO_3^- species were observed at photon energies of ≤407 eV and >407 eV, respectively.

afforded larger concentrations of surface O_α species (≥40.6%) than β-MnO_2. Indeed, α-/γ-MnO_2 reduced their surface O_α concentrations by 5.0−6.5% during NO_Y^- functionalization (Figure 5D). This indicated that O_α species could bind with NO/O_2 and acted as an additional source used to immobilize NO_Y^- species on α-/γ-MnO_2 surfaces.

As a complementary technique of XPS, H_2-TPR experiments were performed to collect the profiles of H_2 consumption versus temperature for the catalysts (Figure S17). H_2-TPR profiles showed a broad band over a wide temperature range of 50−800 °C. This could be deconvoluted into four sub-bands with temperatures centered at ∼215 °C, ∼300 °C, ∼385 °C, and ∼465 °C, each of which could result from O_α species and reductive transition of $Mn^{4+} \rightarrow Mn^{3+}$, $Mn^{3+} \rightarrow Mn^{2+/3+}$, and $Mn^{2+/3+} \rightarrow Mn^{2+}$.[39,81] The areas under the sub-bands assigned to O_α species were quantified for the catalysts and utilized to grasp their O_α concentrations. β-MnO_2 contained negligible O_α contents (∼1.9%), which was in agreement with the analytic result on XPS experiment discussed above. Conversely, α-/γ-MnO_2 included O_α contents of 10−12% and utilized O_α components of 3.5−4.5% for synthesizing α-/γ-MnO_2-N (Figure 5D), which again could originate from the fusion between O_α and NO/O_2 to immobilize NO_Y^- species on the surfaces. Apparently, CO-pulsed chemisorption, XPS, and H_2-TPR experiments demonstrated that the generation of NO_Y^- functionalities on α-/γ-MnO_2 surfaces was of great likelihood and could originate from multiple sources such as Mn^{n+}/NO_Y^- and $O_\alpha/NO/O_2$.

In this regard, EA/XRF (bulk) and XPS (surface) techniques served to better quantify the amounts of NO_Y^- species on α-/γ-MnO_2-N surfaces with the use of their N contents (Figure 5C). The molar ratios of N to Mn (N/Mn) innate to α-MnO_2-N were twice and ∼1.5 times those inherent to γ-MnO_2-N in the bulk and surface scale, respectively. This highly suggested that the generation of $NO_3^{\bullet}{}_{SUP}$ species could be more efficient in the α-MnO_2-N surface than the γ-MnO_2-N surface per unit time, if the $^{\bullet}OH$ productivity of α-MnO_2-N were similar to or greater than that of γ-MnO_2-N. It should also be stressed that the binding configurations of NO_Y^- functionalities and their populations on α-/γ-MnO_2-N surfaces are essential factors to consider and therefore were analyzed via DRIFT and XPS/XANES spectroscopy, respectively. Background-subtracted *in situ* DRIFT spectra of α-/γ-MnO_2 were collected by exposing the surfaces to NO/O_2 stream at 150 °C for an hour to simulate the conditions utilized to functionalize α-/γ-MnO_2 surfaces with NO_Y^- species (Figure 6A).[39] The catalysts showed large bands, which resulted from the N−O bond of NO_3^- coordinated to Mn^{n+}/O_α with *mono-* or *bi*-dentate configuration.[39] The catalysts also exhibited bands, originating from the N−O bond of NO_2^- bound to Mn^{n+}/O_α

https://doi.org/10.1021/jacsau.1c00124
JACS Au 2021, 1, 1158−1177

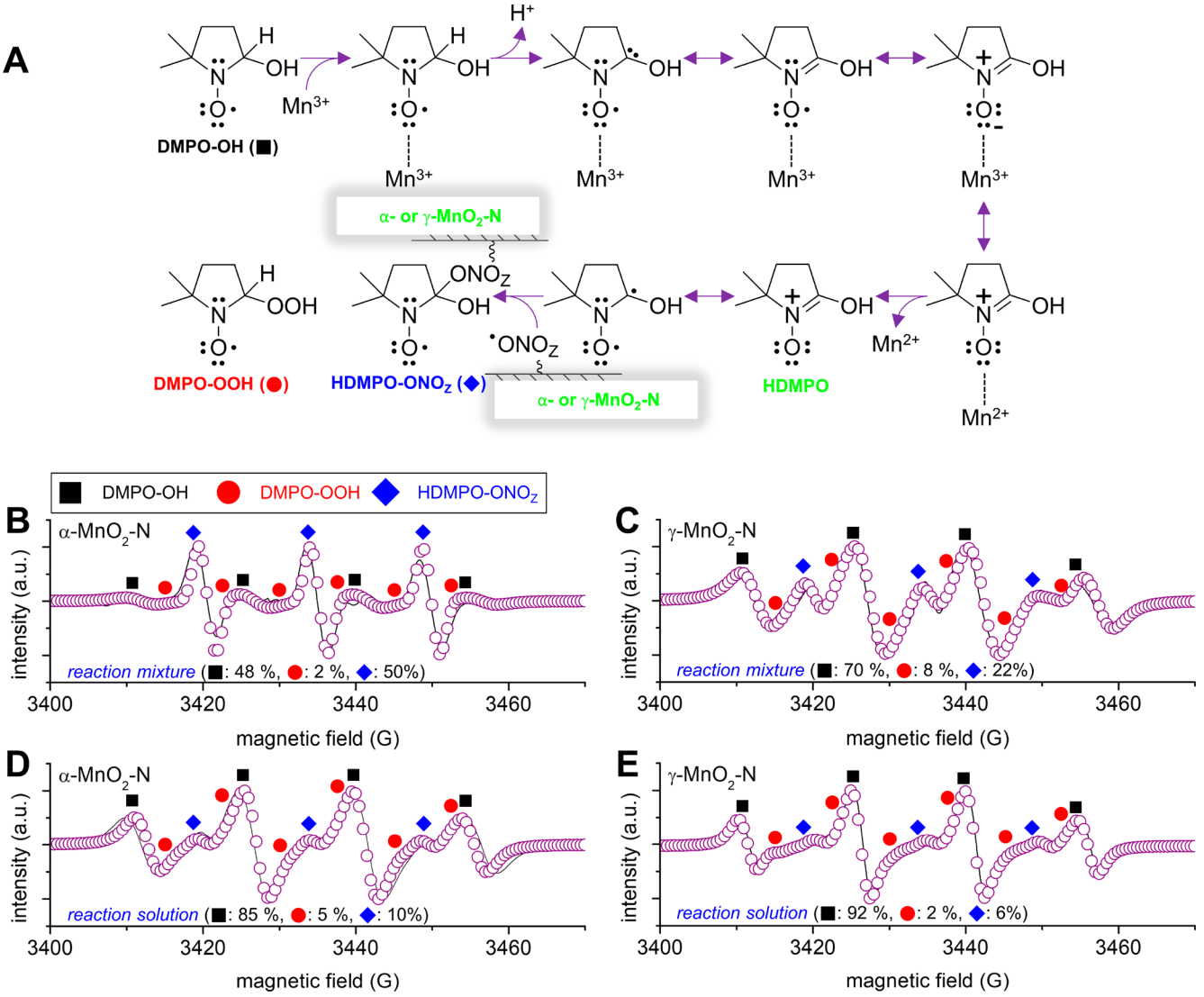

Figure 7. (A) Formation mechanisms of HDMPO-ONO_Z adduct (Z = 1 or 2). EPR spectra of reaction aliquots taken from reaction mixtures (solid (catalyst) + liquid; B and C) or reaction solutions (liquid; D and E). Reaction mixtures contained DMPO as a spin trapper for $^{\bullet}OH/^{\bullet}OOH/O_2^{\bullet-}/NO_2^{\bullet}{}_{SUP}/NO_3^{\bullet}{}_{SUP}$ and α-MnO_2-N (B and D) or γ-MnO_2-N (C and E) as a catalyst. Reaction solutions were obtained from the filtration of reaction mixtures using a 0.45-μm-sized PES syringe (D and E). In parts B–E, black solid lines and empty purple circles indicate raw and simulated EPR spectra, respectively. Black solid squares, red solid circles, and blue solid diamonds indicate DMPO-OH, DMPO-OOH, and HDMPO-ONO_Z adducts, respectively, whose relative abundance was simulated and exhibited in parts B–E. Reaction mixture: 2 mg of the catalyst with the sizes of $\leq$50 μm; 1 mL of deionized H_2O; 0.3 mmol of H_2O_2; 3 mmol of DMPO; pH of 7.0; 25 °C; vortex for 2 min.

with minute intensities.[39] The area under the *in situ* NO/O_2-DRIFT spectrum of α-MnO_2 was greater than that of γ-MnO_2. This corroborated that the α-MnO_2 surface had a greater inclination to be modified by NO_Y^- species than γ-MnO_2, which was also in close alignment with the N/Mn ratios of α-/γ-MnO_2-N elucidated above (Figure 5C). The XP spectra of α-/γ-MnO_2-N in the N 1s domains were further explored via deconvolution to reveal two sub-bands with binding energies centered at ~407.4 eV and ~403.6 eV, each of which was assigned to surface NO_3^- and NO_2^- species (Figure 6B and D).[82] The XP spectral results in the N 1s domains suggested that the α-MnO_2-N surface could provide a higher NO_3^- concentration (80.2%) than the γ-MnO_2-N counterpart (49.6%). However, the XPS results discussed above did show low "signal-to-noise" ratios due possibly to low concentrations of surface N species (Figure 5C) and thus were only partially convincing.

Hence, XANES at the N K-edges also served as an alternative to accurately quantify surface NO_Y^- concentrations innate to α-/γ-MnO_2-N. The XANES curves were divided into two domains of π^* and σ^* resonance at photon energies of $\leq$407 eV and >407 eV, respectively.[83,84] Intense bands found in π^* resonance were deconvoluted into NO_2^- (a in Figure 6C and E) and NO_3^- (b in Figure 6C and E) with photon energies centered at 402.5 and 406.2 eV, respectively.[83,84] NO_2^- and NO_3^- were caused by the electronic transition of 1s → $2b_1$ and 1s → $2a_2''$, respectively,[83,84] with the latter area being larger in α-MnO_2-N (32.1% relative to 2.5%) compared to γ-MnO_2-N (17.6% relative to 26.4%). Additional intense bands found in the σ^* resonance were also deconvoluted into NO_2^- (a′ in Figure 6C and E) and NO_3^- (b′ and b′′ in Figure 6C and E) with photon energies centered at 413.0 and 416.0 eV/418.1 eV, respectively.[83,84] NO_2^- and NO_3^- were caused by electronic excitation to empty orbitals of 1s → $7a_1/5b_2$ and

https://doi.org/10.1021/jacsau.1c00124
JACS Au 2021, 1, 1158–1177

1s → $5a_1'/5e_1'$, respectively,[83,84] with the latter area again being greater in α-MnO_2-N (50.0% relative to 15.4%) compared to γ-MnO_2-N (34.0% relative to 22.0%). XP and XANES spectra provided sound evidence that α-MnO_2-N provided a higher concentration of NO_3^- than γ-MnO_2-N. When considering that $NO_2^•$ is less electrophilic and shorter-lived than $NO_3^•$,[21,22,40] α-MnO_2-N could potentially degrade phenol better than γ-MnO_2-N by having a higher chance to evolve $NO_3^•{}_{SUP}$ species via the $^•OH$ → $NO_3^•{}_{SUP}$ route. Overall, α-MnO_2-N was anticipated to outperform γ-MnO_2-N in degrading phenol because of multiple merits including the smaller Lewis acidic strength of the Mn^{n+} species for promoting $^•OH$ desorption (potential rate-determining stage of $^•OH$ → $NO_3^•{}_{SUP}$ route) and larger N contents/higher NO_3^- concentration for furthering the collisions between $^•OH$ and $NO_3^•{}_{SUP}$ species per unit time.

Viability of $^•OH$ → $NO_3^•$ on α-/γ-MnO_2-N

EPR spectra of reaction mixtures and solutions were then inspected to identify a group of radicals generated such as $^•OH$, $^•OOH/O_2^{•-}$, and $NO_Y^•{}_{SUP}$ under such environments that could mimic $^•OH$ → $NO_Y^•{}_{SUP}$ on α-/γ-MnO_2-N with the inclusion of DMPO as a spin trapper. (See the details in Figure 7 caption.) Of note, given the literature on the transition of DMPO upon its coordination to Fe^{3+},[85] a series of steps were proposed to account for the production of $NO_Y^•{}_{SUP}$ species. Catalytic H_2O_2 scission on surface Mn^{n+} sites initially forms $^•OH$ species, some of which can migrate into supported NO_Y^- functionalities to generate $NO_Y^•{}_{SUP}$ species. In addition, the remaining $^•OH$ species are also coordinated to DMPO to produce DMPO−-OH adducts (black squares in Figure 7A).[72,73,86] Furthermore, catalytic H_2O_2 scission on surface Mn^{n+} sites also produces $^•OOH/O_2^{•-}$ species, both of which are also adducted by DMPO to form DMPO-OOH (red circles in Figure 7A),[72−74,86] as illustrated in Figure 4. Meanwhile, DMPO-OH adducts provide a lone e^- pair of O species allowing for the coordination to surface Mn^{3+} species, liberate H^+, exchange e^- with vicinal Mn^{3+} species for their reduction to Mn^{2+} analogues, and are detached from the resulting Mn^{2+} species. This can lead to the evolution of surface-unbound HDMPO adduct, as highlighted with green in Figure 7A. The resulting HDMPO species are finally bound to $NO_Y^•{}_{SUP}$ species ($ONO_Z^•$ on α-/γ-MnO_2-N in Figure 7A, where Z = 1 or 2) to evolve HDMPO-ONO_Z species supported on α-/γ-MnO_2-N surfaces (blue diamonds in Figure 7A).

Of additional note, a number of six-membered spin adducts, where -H on β-carbon is replaced by -CH_3, were reported to reveal hyperfine splitting constants ($a(^{14}N)$) of 16.1−17.3 G in their EPR spectra. The spin adducts stated above also exhibited trio signals with the intensity ratios of 1:1:1 (See Table S7 with references cited.), as might be the case with supported HDMPO-ONO_Z. In addition, it was also found in previous literature on spin adducts with partial structural similarity to supported HDMPO-ONO_Z that a greater decrease in $a(^{14}N)$ was observed in a five-membered spin adduct, in which a bulkier substituent was replaced for -H on β-carbon, -H on γ/γ'-carbons, or -CH_3 on β'-carbon ($a(^{14}N)$ values of 13.1−14.9 G in Table S7). Hence, HDMPO-ONO_Z species bound to "bulky α-/γ-MnO_2-N" were envisaged to show $a(^{14}N)$ of ∼14.7 G, in addition to assuming $a(^1H)$ of ∼1.1 G for -H on γ-carbon (Table S4). Indeed, the signals originating from DMPO-OH, DMPO-OOH, and supported HDMPO-ONO_Z were detected throughout the EPR spectra (Figure 7B−E). This did indicate that the evolution of $NO_Y^•{}_{SUP}$ on α-/γ-MnO_2-N was of great plausibility via the $^•OH$ → $NO_Y^•{}_{SUP}$ route. The predicted EPR signals of supported HDMPO-ONO_Z were then coupled with those of DMPO-OH/DMPO-OOH and utilized to simulate the EPR spectra. Again, the consideration of DMPO-OOH was imperative to attain good fits between EPR spectra observed and simulated, despite the relative abundance of DMPO-OOH being only 2−8% across the simulated EPR spectra. In addition, although the EPR spectra can only allow for rough comparison of relative abundance among paramagnetic species detected/simulated,[75−77] the intensities of signals assigned to supported HDMPO-ONO_Z species were more pronounced in the EPR spectra of reaction mixtures (solid (catalyst) + liquid; 22−50%) compared to those of the corresponding reaction solutions (liquid; 6−10%), as shown in Figure 7. This indicated that HDMPO-ONO_Z species were present in α-/γ-MnO_2-N surfaces, which could also provide sound evidence concerning the evolution of $NO_Y^•{}_{SUP}$ species via $^•OH$ → $NO_Y^•{}_{SUP}$. It should be noted that reaction solutions also exhibited signals assigned to supported HDMPO-ONO_Z species. This could be due to the inclusion of α-/γ-MnO_2-N particulates with sizes of <0.45 μm in reaction mixtures because a 0.45-μm-sized PES syringe served to isolate reaction solutions from reaction mixtures. Again, the EPR spectral results substantiated that the $^•OH$ → $NO_Y^•{}_{SUP}$ route on α-/γ-MnO_2-N surfaces was highly tangible.

The feasibility of the $^•OH$ → $NO_3^•{}_{SUP}$ route was further investigated via DFT calculations with thermodynamic energy analysis on supported NO_3^- (or $NO_3^•$) species via a cluster model,[26] whose details are provided in the Supporting Information. Herein, $NO_3^•$ (or NO_3^-) was chosen because of its merits over $NO_2^•$ in terms of reduction potential and lifetime,[21,22,40] as stated above. On the other hand, the (110) facet was selected due to its thermodynamic stability and ubiquity across α-/β-/γ-MnO_2 architectures. Initially, gaseous NO_3^- was attempted to be intercalated into the pores normal to (110) facets for relaxed α-/β-/γ-MnO_2 structure models. The diffusion of NO_3^- species into the pores of MnO_2, however, was readily achievable in the α-MnO_2 architecture (Figure S18A), thus rationalizing the selection of α-MnO_2 for further calculations. The surface-terminated (110) facet of α-MnO_2 was then subjected to the removal of an O atom coordinated to two surface Mn species and optimized (¥ in Figure S18B). This led to the creation of two Mn defects utilized to interact with an O atom of NO_3^-, as shown in Figure 8A. The energy required for two O atoms of NO_3^- to bind with defective Mn species (blue dashed circles in Figure 8) was highly exothermic, as evidenced by the calculated adsorption energy of -3.0×10^3 kJ mol^{-1} ($\Delta E_{NO3\text{-}ADSORPTION} = E_{NO3\text{-}ON\ \alpha\text{-}MnO2\text{-}N} - (E_{NO3\text{-}} + E_{\alpha\text{-}MnO2})$). It was also identified via calculations that NO_3^- could settle down in the surface-terminated (110) facet for α-MnO_2 via a bridging *bi*-dentate configuration in the most stable fashion, while leaving an O atom highly active in degrading pollutants. This could be coupled with *in situ* NO/O_2-DRIFT spectral results on α-/γ-MnO_2 (Figure 6A), in which the bands originating from surface NO_3^- species with *bi*-dentate arrays were more pronounced in the α-MnO_2 surface, thereby deriving the tentative conclusion that α-MnO_2-N outperformed γ-MnO_2-N in accelerating $^•OH$ → $NO_3^•{}_{SUP}$ per unit time.

Of interest, the length of the N−O bonds for surface-unbound NO_3^- was calculated to be 1.44 Å yet was reduced to

https://doi.org/10.1021/jacsau.1c00124
JACS Au 2021, 1, 1158−1177

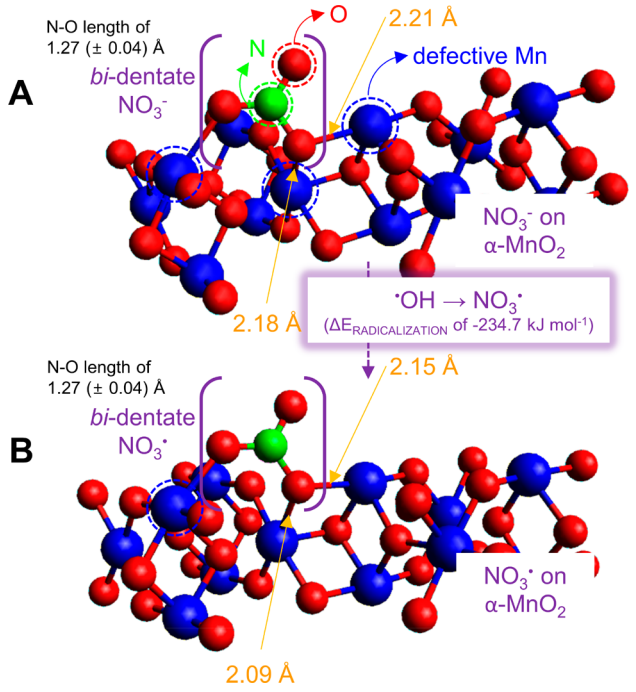

Figure 8. Computed surface (110) facet of α-MnO_2 with defective Mn species (shown with blue dashed circles) coordinated to NO_3^- (A) or $NO_3^\bullet$ (B) via *bi*-dentate configurations.

~1.27 Å upon the adsorption of NO_3^- on α-MnO_2 and retained during the radicalization of NO_3^- on α-MnO_2-N upon structural relaxation (Figure 8B). This indicated e^- extraction from supported NO_3^- could incur only a little structural deformation in the resulting $NO_3^\bullet{}_{SUP}$. This also suggested $^\bullet OH \rightarrow NO_3^\bullet{}_{SUP}$ could be highly favorable, which was in partial line with rapid $^\bullet OH$-mediated radicalization of NO_3^- ion ($^\bullet OH \rightarrow NO_3^\bullet$) with a k of ~10^5–10^8 M^{-1} s^{-1}.[15,16] Of additional interest, the radicalization of supported NO_3^- could shorten the lengths of N–O bonds bound to defective Mn species from 2.18 to 2.21 Å to 2.09–2.15 Å. This highly suggested that $NO_3^\bullet$ species could be coordinated to α-MnO_2 more rigidly than NO_3^- counterparts. Indeed, the energy released for the radicalization of NO_3^- on α-MnO_2-N was computed to unveil 234.7 kJ mol^{-1} ($\Delta E_{RADICALIZATION} \sim (E_{NO3\bullet \text{ on } \alpha\text{-MnO2-N}} + E_{OH\text{-}}) - (E_{NO3\text{-on } \alpha\text{-MnO2-N}} + E_{OH\bullet})$ in Figure 8). In conjunction with the EPR spectral results discussed above, the calculation results could prove that the formation of $NO_3^\bullet{}_{SUP}$ species was of substantial energetic favor. In addition to our validation that $^\bullet OH$ desorption was the rate-determining step of the H_2O_2 scission cycle on α-/β-/γ-MnO_2, the exothermic nature of $NO_3^\bullet{}_{SUP}$ production could also prove that $^\bullet OH$ desorption from α-/γ-MnO_2-N was the rate-determining stage of the $^\bullet OH \rightarrow NO_3^\bullet{}_{SUP}$ route which the H_2O_2 scission cycle is part of. This was in close alignment with the conclusion derived in our previous studies concerning the $^\bullet OH \rightarrow SO_4^{\bullet-}{}_{SUP}$ route, where $^\bullet OH$ desorption was endothermic and thus directed the overall $^\bullet OH \rightarrow SO_4^{\bullet-}{}_{SUP}$ route as the rate-determining step, whereas $SO_4^{\bullet-}{}_{SUP}$ formation was exothermic.[27,28]

$OH \rightarrow NO_3^\bullet$ Kinetics on α-/γ-MnO_2-N

H_2O_2 scission/phenol decomposition runs on α-/γ-MnO_2-N were then performed identically to those on α-/β-/γ-MnO_2

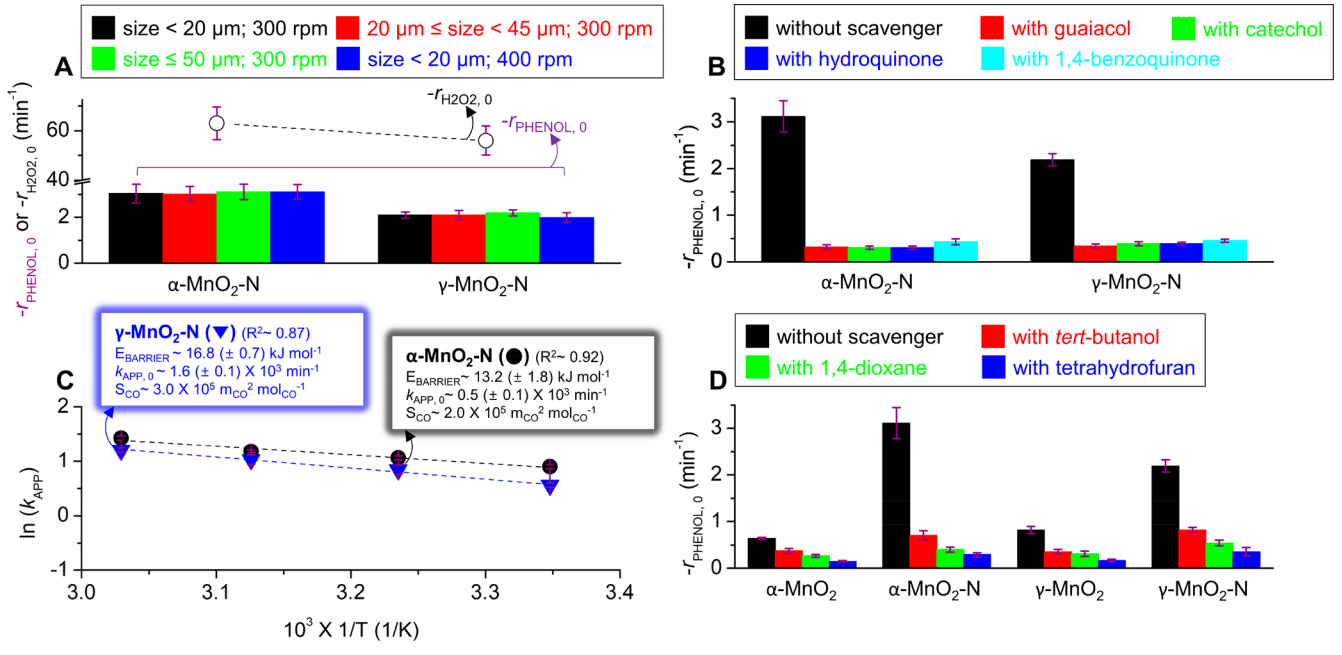

Figure 9. (A) Background-subtracted $-r_{H2O2,0}$ and $-r_{PHENOL,0}$ values of α-MnO_2-N and γ-MnO_2-N, for which particle size or stirring speed was varied during phenol decomposition runs. Change in $-r_{PHENOL,0}$ values for the catalysts in the absence or the presence of quencher (guaiacol, catechol, hydroquinone, or 1,4-benzoquinone for B; *tert*-butanol, 1,4-dioxane, or tetrahydrofuran for D). (C) Arrhenius plots ($\ln(k_{APP})$ versus 10^3/T) for α-MnO_2-N and γ-MnO_2-N, whose apparent reaction rate constants (k_{APP}) were obtained from phenol decomposition runs at 25~55 °C. Reaction conditions: 0.2 g of the catalysts with the sizes of ≤50 μm (H_2O_2 scission (A), B, C, and D) or <20 μm/20–45 μm/≤ 50 μm (phenol decomposition (A)); 100 mL of deionized H_2O; 30 mmol of H_2O_2; 0 mmol (H_2O_2 scission (A)) or 0.1 mmol of phenol (phenol decomposition (A), B, C, and D); quencher of 0 mmol (A and C), 60.0 mmol for α-MnO_2 and γ-MnO_2, 60.2 mmol for α-MnO_2-N, and 60.1 mmol for γ-MnO_2-N (B and D); pH of 7.0; 25 °C (A, B, and D) or 25~55 °C (C); 300 rpm (H_2O_2 scission (A), B, C, and D) or 400 rpm (phenol decomposition (A)).

https://doi.org/10.1021/jacsau.1c00124
JACS Au 2021, 1, 1158–1177

(Figures S8 and S10), whereas the resulting $-r_{H2O2,0}/-r_{PHENOL,0}$ values were corrected using the backgrounds specified above.[26−28] The $-r_{H2O2,0}$ values of α-/γ-MnO_2-N were 1.5−2.5-fold higher than those of α-/γ-MnO_2 (Figure 9A). This could validate the merit of NO_Y^- functionalities potentially acting as e^- donators to vicinal Mn^{n+} species, which could in turn weaken their Lewis acidic strengths, resulting in the promotion of $^{\bullet}OH$ desorption efficiency per unit time. In addition, $-r_{H2O2,0}$ of α-MnO_2-N was ∼10 min^{-1} greater than that of γ-MnO_2-N (∼55 min^{-1}). This might suggest α-MnO_2-N enhances $^{\bullet}OH \rightarrow NO_3^{\bullet}{}_{SUP}$ efficiency over γ-MnO_2-N, as also anticipated based on the AOS values of surface Mn species andthe $-Q_{ST,CO2}$ values for α-/γ-MnO_2-N.

The $-r_{PHENOL,0}$ values of α-/γ-MnO_2-N were also assessed with the variation of catalyst particle sizes and/or stirring speeds to ensure negligible effects of internal/external diffusions on $-r_{PHENOL,0}$ values (Figure 9A).[27] Similar to the $-r_{PHENOL,0}$ values of α-/β-/γ-MnO_2 (Figure 3A), the $-r_{PHENOL,0}$ values of α-/γ-MnO_2-N were invariant even with the change in reaction conditions mentioned above. This indicated that the interactions between H_2O_2 and Mn^{n+}, $^{\bullet}OH$ and supported NO_3^-, $NO_3^{\bullet}{}_{SUP}$ and phenol were not limited by diffusional artifacts across the catalysts. In addition to the exothermic nature of the radical interconversion stages on $^{\bullet}OH \leftrightarrow NO_3^{\bullet}{}_{SUP}$ elucidated via DFT calculations, this could leave $^{\bullet}OH$ desorption as the rate-determining stage of the overall $^{\bullet}OH \rightarrow NO_3^{\bullet}{}_{SUP}$ route for α-/γ-MnO_2-N. Of significance, the $-r_{PHENOL,0}$ values of α-/γ-MnO_2-N were 2.5−5.0-fold higher than those of α-/γ-MnO_2 (Figure 9A), which demonstrated that $NO_3^{\bullet}{}_{SUP}$ could outperform conventional $^{\bullet}OH$ in degrading phenol. Although α-/γ-MnO_2-N barely leached N species ($\leq 10^{-4}$ mol %) after 8 h of reaction runs, α-MnO_2-N lost Mn species markedly (∼5.2 mol %) compared to γ-MnO_2-N (∼0.1 mol %). This posed the need of synthetic amendment used to reduce Mn leaching from the α-MnO_2-N surface. Nonetheless, the $-r_{PHENOL,0}$ of α-MnO_2-N was ∼1.0 min^{-1} higher than that of γ-MnO_2-N and showed the largest $-r_{PHENOL,0}$ among the catalysts studied. This suggested that α-MnO_2 could be most suitable to desorb $^{\bullet}OH$ and afford surface NO_3^- species, which were combined to improve the $^{\bullet}OH \rightarrow NO_3^{\bullet}{}_{SUP}$ efficiency on α-MnO_2-N, as also supported by computations, EA/XRF, XPS, XANES experiments, etc.

Filtration runs on α-/γ-MnO_2-N were carried out following the identical protocols to those used to conduct filtration runs on α-/β-/γ-MnO_2, whose details were discussed above.[26−28] Again, the objective of filtration runs was to verify the significance of surface-unbound, leached Mn species ($^{\bullet}OH$ producer) present in reaction solutions on phenol degradation performance. Thus, the ΔX_{PHENOL} values of reaction solutions (liquid) were evaluated at 1−8 h of reaction runs upon their separation from reaction mixtures (solid (catalyst) + liquid) via vacuum filtration after an hour of reaction runs. ΔX_{PHENOL} of the reaction solution in the absence of the catalyst was 4.3 (±0.5) % ($\Delta X_{PHENOL,BLANK}$), which again primarily resulted from H_2O_2 self-decomposition.[26−28,71] The $\Delta X_{PHENOL,BLANK}$ value was comparable to the ΔX_{PHENOL} value of the reaction solution separated from the reaction mixture including α-MnO_2-N (5.3 (±0.6) %) or γ-MnO_2-N (4.3 (±1.0) %), as shown in Figure S13. This did suggest that α-MnO_2-N (or γ-MnO_2-N) could decompose phenol with the main use of $NO_3^{\bullet}{}_{SUP}$ species instead of surface-unbound $^{\bullet}OH$ tentatively produced via H_2O_2 scission on leached Mn species, albeit the amount of Mn species leached from α-MnO_2-N was not trivial.

To clearly identify the major degrader of phenol on α-/γ-MnO_2-N, scavenging runs were performed identically to those on α-/β-/γ-MnO_2 (Figures S12 and S19).[26−28] The quantities of quenchers used during the reactions were around twice the amounts of H_2O_2 coupled with the N species of the catalysts present in the reaction mixtures.[26−28] Guaiacol, catechol, hydroquinone, or 1,4-benzoquinone served as a quencher to terminate $^{\bullet}OH$, $^{\bullet}OOH$, $O_2^{\bullet-}$, $NO_3^{\bullet}{}_{SUP}$, or $NO_2^{\bullet}{}_{SUP}$ with a wide range of secondary rate constants in terminating the radicals stated above (k_{XXX}, where XXX denotes the radical in Table S6 with references cited). If the prime degrader of phenol were $NO_2^{\bullet}{}_{SUP}$,$-r_{PHENOL,0}$, values of α-/γ-MnO_2-N should be maintained even with the addition of hydroquinone ($k_{NO2\bullet}$ of 0 M^{-1} s^{-1}) into reaction mixtures. However, α-/γ-MnO_2-N reduced their $-r_{PHENOL,0}$ values markedly in the presence of hydroquinone (Figure 9B), which allowed for the conclusion that $NO_2^{\bullet}{}_{SUP}$ functioned as a minor species in decomposing phenol. In addition, hydroquinone ($k_{\bullet OOH}$ of 1.7 × 10^7 M^{-1} s^{-1}) can terminate $^{\bullet}OOH$ around ∼10^3 faster than catechol ($k_{\bullet OOH}$ of 4.7 × 10^4 M^{-1} s^{-1}). $-r_{PHENOL,0}$ values of α-/γ-MnO_2-N stayed under similar magnitudes upon the change in the type of scavengers from catechol to hydroquinone (Figure 9B), which indicated that the function of $^{\bullet}OOH$ as the main phenol decomposer was highly unlikely. Furthermore, the difference in terminating $O_2^{\bullet-}$ was quite dissimilar across the scavengers utilized, as evidenced by the difference in their $k_{O2\bullet-}$ values of ∼6 orders of magnitude (Table S6). Hence, if $O_2^{\bullet-}$ were the prime decomposition product of phenol, the $-r_{PHENOL,0}$ values of α-/γ-MnO_2-N should be significantly distinct and decrease in the following order of guaiacol (2.5 × 10^3 M^{-1} s^{-1}) → catechol (2.7 × 10^5 M^{-1} s^{-1}) → hydroquinone (1.7 × 10^7 M^{-1} s^{-1}) → 1,4-benzoquinone (1.0 × 10^9 M^{-1} s^{-1}). Nonetheless, the $-r_{PHENOL,0}$ values of α-/γ-MnO_2-N varied by less than an order of magnitude only, regardless of altering the type of scavengers utilized (Figure 9B), which validated that $O_2^{\bullet-}$ acted as a minor species in degrading phenol. This left $^{\bullet}OH$ or $NO_3^{\bullet}{}_{SUP}$ as the tentative main degrader of phenol. It should be noted that guaiacol, catechol, and hydroquinone could be barely distinct in quenching $^{\bullet}OH$ or $NO_3^{\bullet}{}_{SUP}$ species because their $k_{\bullet OH}$ or $k_{NO3\bullet}$ values only differ by less than an order of magnitude (Table S6).

Therefore, *tert*-butanol, 1,4-dioxane, or tetrahydrofuran served as additional quenchers to identify the prime decomposer of phenol by monitoring their effects on the $-r_{PHENOL,0}$ values for α-/γ-MnO_2-N, whereas the $-r_{PHENOL,0}$ values of α-/γ-MnO_2 were also presented in Figure 9D for comparison with those of α-/γ-MnO_2-N. It was found that the $-r_{PHENOL,0}$ values of α-/γ-MnO_2 were reduced in the following order of *tert*-butanol →1,4-dioxane → tetrahydrofuran, which was in exact agreement with the increasing trend of $k_{\bullet OH}$ or $k_{NO3\bullet}$ values for the quenchers utilized (Figure 9D and Table S6). Of note, $k_{\bullet OH}$ of *tert*-butanol, 1,4-dioxane, or tetrahydrofuran was 10^2−10^4-fold larger than its $k_{NO3\bullet}$ counterpart. Hence, if $^{\bullet}OH$ were the main degrader of phenol, the $-r_{PHENOL,0}$ of α- or γ-MnO_2-N could be of similar magnitude to or even smaller than that of α-or γ-MnO_2 in the presence of the quencher mentioned above. However, the $-r_{PHENOL,0}$ of α- or γ-MnO_2-N was always higher than that of α- or γ-MnO_2 in the presence of the identical scavenger (Figure 9D). This suggested that $NO_3^{\bullet}{}_{SUP}$ species could play a major role in degrading phenol on α-/γ-MnO_2-N. Of additional note, the $-r_{PHENOL,0}$ values of α-/γ-MnO_2 in the presence of scavengers

https://doi.org/10.1021/jacsau.1c00124
JACS Au 2021, 1, 1158−1177

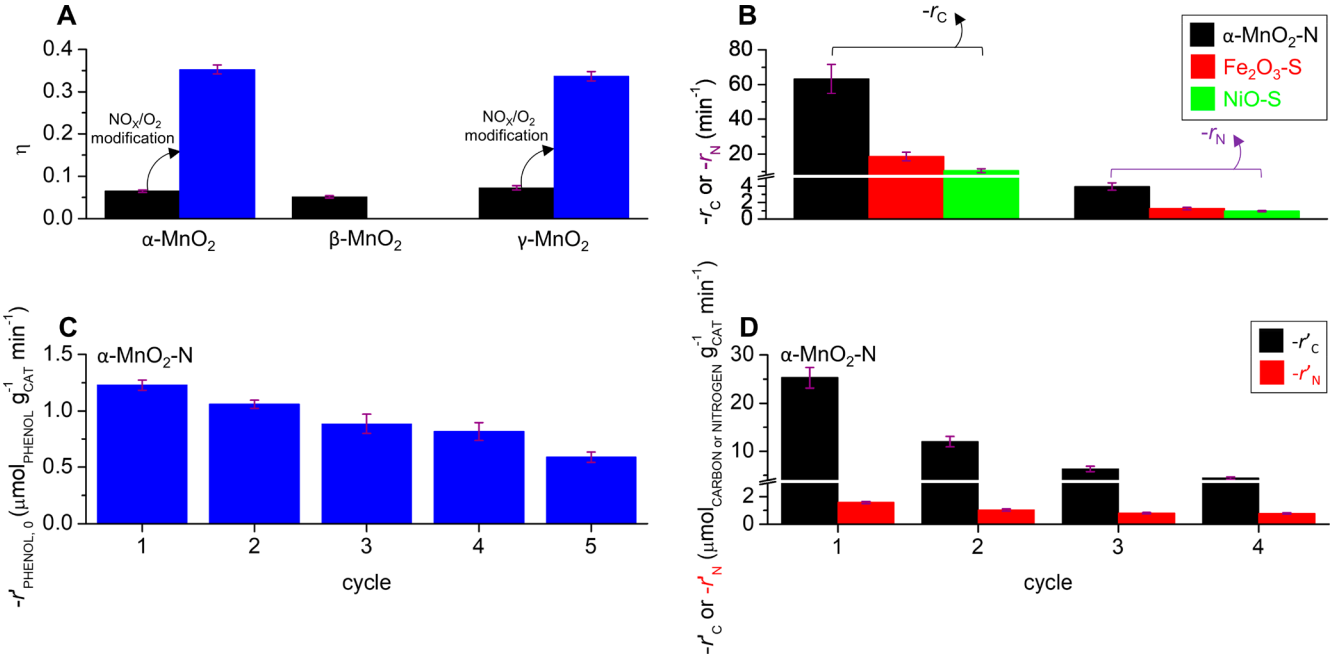

Figure 10. (A) Mineralization efficiencies (η) of the catalysts in decomposing phenol. (C) Background-subtracted initial phenol decomposition rates ($-r'_{PHENOL,\,0}$) for as-synthesized (1st cycle) or used α-MnO_2-N catalysts (2nd∼5th cycles). (B) Background-subtracted initial degradation rates of textile wastewater for α-MnO_2-N, Fe_2O_3−S, and NiO-S in terms of carbon ($-r_C$) or nitrogen component ($-r_N$). (D) Background-subtracted initial degradation rates of textile wastewater ($-r'_C$ and $-r'_N$) for as-synthesized (1st cycle) or used α-MnO_2-N catalysts (2nd∼4th cycles). Reaction conditions for (C): 0.2 g of α-MnO_2-N (as-synthesized or used) with the sizes of ≤50 μm; 100 mL of deionized H_2O; 30 mmol of H_2O_2; 0.1 mmol of phenol; pH of 7.0; 25 °C; 300 rpm. Reaction conditions for (B) and (D): 2 g of the catalysts (as-synthesized or used) with the sizes of ≤50 μm; 200 mL of textile wastewater undergoing vacuum filtration with 1.2 μm GF/C filter paper; 150 mmol of H_2O_2; pH of 7.0; 25 °C; 300 rpm.

($\Delta-r_{PHENOL,0}$) only differed by 0.5−0.7 min^{-1}, which was highly anticipated given the difference among the $k_{\bullet OH}$ values of the scavengers used (less than an order of magnitude). Conversely, $\Delta-r_{PHENOL,0}$ of α-/γ-MnO_2-N was 1.8−2.8 min^{-1} and far larger than that of α-/γ-MnO_2 (Figure 9D). Considering the difference among the $k_{NO3\bullet}$ values of the scavengers utilized (3 orders of magnitude), one could conclude that $NO_3^{\bullet}{}_{SUP}$ species were the prime degrader of phenol.

Arrhenius plots of α-/γ-MnO_2-N were finally constructed to compare their kinetic parameters (Figures 9C and S14).[26−28] Again, the Lewis acidic strength of Mn^{n+} species inherent to α-MnO_2-N was smaller than that innate to γ-MnO_2-N. Thus, α-MnO_2-N was expected to accelerate the rate-determining stage ($^{\bullet}OH$ desorption) more readily than γ-MnO_2-N. Indeed, this could be corroborated by the smaller $E_{BARRIER}$ of α-MnO_2-N (∼13.2 kJ mol^{-1}) compared to that of γ-MnO_2-N (∼16.8 kJ mol^{-1}).

Meanwhile, the collision frequency between H_2O_2 and Mn^{n+} could be greater in γ-MnO_2-N in comparison with α-MnO_2-N. This could be evidenced by a larger surface area of Lewis acidic Mn^{n+} species innate to γ-MnO_2-N (S_{CO} of ∼3.0 × 10^5 m_{CO}^2 mol_{CO}^{-1}) than that of α-MnO_2-N (S_{CO} of ∼2.0 × 10^5 m_{CO}^2 mol_{CO}^{-1}; Figure S7). Conversely, α-MnO_2-N could enhance the collision frequency between $^{\bullet}OH$ and NO_3^- over γ-MnO_2-N, as supported by a greater N content (via EA/XRF/XPS) and a larger concentration of NO_3^- relative to that of NO_2^- (via XPS/XANES) in conjunction with a higher $^{\bullet}OH$ productivity (via $-r_{H2O2,0}$). However, the prefactor ($k_{APP,0}$) of γ-MnO_2-N (∼1.6 × 10^3 min^{-1}) was larger than that of α-MnO_2-N (∼0.5 × 10^3 min^{-1}). This suggested that H_2O_2···Mn^{n+} interactions could outweigh $^{\bullet}OH$···NO_3^- counterparts in improving the recurrence of $^{\bullet}OH \rightarrow NO_3^{\bullet}{}_{SUP}$ per unit time. Nonetheless, $-r_{PHENOL,0}$ values of α-MnO_2-N were consistently greater than those of γ-MnO_2-N throughout all temperature domains considered. This made it persuasive that the core in promoting the $^{\bullet}OH \rightarrow NO_3^{\bullet}{}_{SUP}$ route is to facilitate $^{\bullet}OH$ desorption for lowering $E_{BARRIER}$ and that the α-MnO_2 geometry is the optimum to exploit the $^{\bullet}OH \rightarrow NO_3^{\bullet}{}_{SUP}$ route upon NO_3^- functionalization.

Merits of $NO_3^{\bullet}{}_{SUP}$ over $^{\bullet}OH/SO_4^{\bullet-}{}_{SUP}$

$NO_3^{\bullet}{}_{SUP}$ on α-/γ-MnO_2-N did reveal a higher $-r_{PHENOL,0}$ than $^{\bullet}OH$ liberated from α-/γ-MnO_2, albeit α-/γ-MnO_2-N leached a larger or comparable quantity of Mn species compared to α-/γ-MnO_2. Hence, the advantage of $NO_3^{\bullet}{}_{SUP}$ over conventional $^{\bullet}OH$ was further explored using the conversion (X) ratios of X_{CARBON} to X_{PHENOL} (X_{CARBON}/X_{PHENOL} analyzed via TOC/HPLC techniques in eqs S10 and S5).[28,60] This corresponded to the mineralization efficiencies of the catalysts (η) to assess the portions of phenol that underwent mineralization after 8 h of reaction runs (Figures 10A and S10).[28,60] The η values of α-/γ-MnO_2-N (∼0.35) were 5−7-fold larger than those of α-/β-/γ-MnO_2 (<0.1), thereby corroborating that $NO_3^{\bullet}{}_{SUP}$ outperformed conventional $^{\bullet}OH$ in the mineralization of phenol. α-/γ-MnO_2-N exhibited comparable η values yet could be distinct in terms of the Lewis acidic strength of Mn^{n+} ($^{\bullet}OH$ producer), the concentration of NO_3^- ($NO_3^{\bullet}{}_{SUP}$ precursor), $-r_{PHENOL,0}$, and $E_{BARRIER}$, leading to the conclusion that α-MnO_2 could be better than γ-MnO_2 in bearing Mn^{n+}/NO_3^- species and deploying the $^{\bullet}OH \rightarrow NO_3^{\bullet}{}_{SUP}$ route upon NO_3^- functionalization. α-MnO_2-N was thus subjected to phenol decomposition multiple times to test the recyclability of $NO_3^{\bullet}{}_{SUP}$ species (Figure S20), for which α-MnO_2-N was rinsed with deionized H_2O and dried prior to performing the

https://doi.org/10.1021/jacsau.1c00124
JACS Au 2021, 1, 1158−1177

next recycle run. In addition, phenol decomposition efficiencies were evaluated per mass basis to diagnose the practicability of α-MnO_2-N ($-r'_{PHENOL,0}$ in eq S7). The $-r'_{PHENOL,0}$ of α-MnO_2-N was ~1.2 $\mu mol_{PHENOL}\ g_{CAT}^{-1}\ min^{-1}$ at the first cycle yet steadily decreased to ~0.6 $\mu mol_{PHENOL}\ g_{CAT}^{-1}\ min^{-1}$ at the fifth cycle (Figure 10C). This could suggest a moderate recyclability of α-MnO_2-N (or $NO_3^{\bullet}{}_{SUP}$) in degrading phenol. In the meantime, the amount of Mn species leached from α-MnO_2-N was also moderate and varied dynamically such as ~5.2 mol %, ~0.8 mol %, ~1.4 mol %, and ~5.2 mol % at the first, second/third, fourth, and fifth cycles, respectively, with negligible quantities of N species leached ($\leq 10^{-4}$ mol %). However, the trend found in the amounts of $^{\bullet}OH$ producer (Mn) or $NO_3^{\bullet}$ precursor (N) leached from α-MnO_2-N during the recycle run was discrepant to the trend found in its $-r'_{PHENOL,0}$ values observed. In conjunction with the result on the filtration run of α-MnO_2-N, this could suggest that phenol degradation on α-MnO_2-N could be mainly directed by $NO_3^{\bullet}{}_{SUP}$ species.

To further demonstrate the significance of the $NO_3^{\bullet}{}_{SUP}$ species in degrading phenol throughout each of the recycle runs, the XRF/EA and XPS techniques served to inspect the bulk and surface molar ratios of N to Mn (N/Mn) for the used catalysts. The bulk N/Mn values of the catalysts (0.06 (±0.01)) were retained even post experiencing multiple phenol degradation runs (Figure S21B). This was in exact alignment with the surface N/Mn counterparts of the catalysts exhibiting 0.14 (±0.02) throughout the recycle runs (Figure S21B). Meanwhile, the surface NO_3^- concentrations of the used catalysts were also explored using their XP spectra in the N 1s domains, in which the relative abundances of the NO_3^- species were alike throughout the recycle runs (78.8−80.2% in Figure S22). These were combined with minute leaching of N contents from the used catalysts to suggest high likelihood of surface NO_3^- species radicalized by $^{\bullet}OH$ to produce $NO_3^{\bullet}{}_{SUP}$ species during the recycle runs. In contrast, the N_{CO} values of the (used) catalysts were continuously declined after each of the recycle runs (~0.39 $\mu mol_{CO}\ g_{CAT}^{-1}$ for pristine → ~0.16 $\mu mol_{CO}\ g_{CAT}^{-1}$ after the fourth cycle in Figure S21A). This was in agreement with the XP spectra of the (used) catalysts in the Mn $2p_{3/2}$ regimes, where the surface concentration of the $Mn^{2+/3+}$ species steadily declined (~14.7% for pristine → ~8.6% after the fourth cycle in Figure S22). This could highly suggest that the evolution of the $NO_3^{\bullet}{}_{SUP}$ species can be sustainable during multiple recycle runs yet is limited by the $^{\bullet}OH$ species produced via catalytic H_2O_2 scission. This raised the need to tune the synthetic conditions for dispersing ample H_2O_2 activators ($Mn^{2+/3+}$) on an α-MnO_2-N surface.

Textile wastewater with initial TOC, TN, and pH values of ~53 $mmol_{CARBON}\ L^{-1}$, ~6 $mmol_{NITROGEN}\ L^{-1}$, and ~11 further served to compare the practicability of α-MnO_2-N along with SO_4^{2-}-functionalized Fe_2O_3 (Fe_2O_3−S) and NiO (NiO-S), whose synthetic protocols were optimized to enable the $^{\bullet}OH$ → $SO_4^{\bullet-}{}_{SUP}$ route and utilize $SO_4^{\bullet-}{}_{SUP}$ as the main degrader of phenol.[26−28] (See the Supporting Information for details.) Notably, textile wastewater was initially subjected to vacuum filtration to eliminate suspended solids (≥1.2 μm) acting as notorious poisons of catalyst surfaces,[87,88] whereas the pH of the textile wastewater was set to ~7 using H_2SO_4 for the removal of CO_3^{2-}/HCO_3^- ions functioning as a $^{\bullet}OH$ scavenger.[89,90] Textile wastewater degradation runs on α-MnO_2-N, Fe_2O_3−S, and NiO-S were conducted to evaluate their initial degradation rates ($-r_C/-r_N$ in eqs S11 and S12), whose details are provided in the Supporting Information and the Figure S23 caption. The $-r_C/-r_N$ values were defined as the moles of C/N contents consumed per Lewis acidic site per unit time upon the correction using backgrounds such as H_2O_2 self-decomposition and pollutants' adsorption (Figure S23).[26−28] Importantly, $NO_3^{\bullet}{}_{SUP}$ was demonstrated to degrade textile wastewater far more efficiently than $SO_4^{\bullet-}{}_{SUP}$. This was evidenced by the $-r_C$ (~65 min^{-1}) and $-r_N$ values (~4 min^{-1}) of α-MnO_2-N, both of which were higher than those of Fe_2O_3-S and NiO-S ($-r_C$ values of ≤~20 min^{-1}; $-r_N$ values of ≤ ~1 min^{-1} in Figure 10B), while similarly leaching metal components during half an hour of reaction runs (≤~0.5 mol %). This could prove the superiority of $NO_3^{\bullet}{}_{SUP}$ relative to $SO_4^{\bullet-}{}_{SUP}$ in decomposing real wastewater. Finally, α-MnO_2-N was exposed to degradation environments of textile wastewater multiple times to examine its recyclability with the use of the initial degradation rates assessed per mass basis ($-r'_C/-r'_N$ in eqs S13 and S14). The resulting $-r'_C/-r'_N$ values of α-MnO_2-N were gradually reduced to show a sixth and half of their initial values at the fourth cycle (Figure 10D), respectively. This could be due in part to suspended solids (<1.2 μm) present in textile wastewater subjected to vacuum filtration, which were continuously accumulated on/near Mn^{n+} and NO_3^- species throughout each of the recycle runs, resulting in severe decline in their access to H_2O_2 and $^{\bullet}OH$/phenol, respectively, at the fourth cycle. This could be partially substantiated by the continuous decrease in the N_{CO} values of the (used) catalysts throughout each of the recycle runs (~0.39 $\mu mol_{CO}\ g_{CAT}^{-1}$ for pristine; ~0.20 $\mu mol_{CO}\ g_{CAT}^{-1}$ after the first cycle; ~0.13 $\mu mol_{CO}\ g_{CAT}^{-1}$ after the second cycle; ~0.11 $\mu mol_{CO}\ g_{CAT}^{-1}$ after the third cycle). Nevertheless, α-MnO_2-N leached negligible quantities of Mn species from the second cycle (for 30 min; ~0.5 mol % and ~0.1 mol % at the first and the second to fourth cycles). A series of reaction runs were gathered to derive the conclusion that in comparison with conventional $^{\bullet}OH$ and $SO_4^{\bullet-}{}_{SUP}$, $NO_3^{\bullet}{}_{SUP}$ is particularly promising as the decomposer of refractory aqueous contaminants.

CONCLUSIONS

This study has exploited polymorphic MnO_2 as a platform to bear Lewis acidic $Mn^{2+/3+}$ species and NO_3^- functionalities on the surfaces. $Mn^{2+/3+}$ species served to cleave H_2O_2 for the production of surface-unbound $^{\bullet}OH$ species, which in turn could interact with NO_3^- functionalities in proximity, enabling radical interconversion of $^{\bullet}OH \leftrightarrow NO_3^{\bullet}$ (or denoted as $^{\bullet}OH \rightarrow NO_3^{\bullet}$), resulting in the evolution of supported $NO_3^{\bullet}$ ($NO_3^{\bullet}{}_{SUP}$) species deployed to fragment aqueous pollutants (phenol or textile wastewater).

α-/β-/γ-MnO_2 polymorphs provide distinct structural traits. Hence, α-/β-/γ-MnO_2 polycrystallites synthesized herein were hypothesized to afford defective $Mn^{2+/3+}$ species with diverse Lewis acidic strengths, which are vital to direct the rate-determining step ($^{\bullet}OH$ desorption) of the H_2O_2 scission cycle and initial reaction rates in cleaving H_2O_2 ($-r_{H2O2,0}$) or decomposing phenol ($-r_{PHENOL,0}$). Indeed, $Mn^{2+/3+}$ species inherent to α-/β-/γ-MnO_2 acted as the major species in cleaving H_2O_2, resulting in the liberation of $^{\bullet}OH/^{\bullet}OOH/O_2^{\bullet-}$ into aqueous environments, as evidenced by EPR spectra observed/simulated. Of note, filtration runs corroborated that surface-unbound $Mn^{2+/3+}$ species leached from α-/β-/γ-MnO_2 surfaces did function as minor species in producing $^{\bullet}OH/^{\bullet}OOH/O_2^{\bullet-}$, among which $^{\bullet}OH$ was identified to

https://doi.org/10.1021/jacsau.1c00124
JACS Au 2021, 1, 1158−1177

primarily decompose phenol, as substantiated by scavenging runs. Of additional note, $Mn^{2+/3+}$ species innate to γ-MnO_2 were verified to possess the smallest Lewis acidic strengths, thus exhibiting the greatest $-r_{H2O2,0}$ and $-r_{PHENOL,0}$ values among α-/β-/γ-MnO_2.

Meanwhile, α-/β-/γ-MnO_2 surfaces might exhibit high affinity to NO_3^- species and therefore were modified by NO/O_2 to immobilize surface NO_3^- functionalities on α-/γ-MnO_2, denoted as α-/γ-MnO_2-N. It should be stressed that β-MnO_2 barely underwent the modification with NO_3^- species due to its small pore size, as also demonstrated by DFT calculations, thus being excluded for further inspection. XPS and CO_2 isotherm experiments provided evidence that $Mn^{2+/3+}$ species innate to α-/γ-MnO_2-N were less Lewis acidic than those inherent to α-/γ-MnO_2, thus enhancing $-r_{H2O2,0}$ values for α-/γ-MnO_2-N. In addition, α-MnO_2-N provided smaller Lewis acidity than γ-MnO_2-N and thus could expedite the rate-determining stage of the $^{\bullet}OH \rightarrow NO_3^{\bullet}$ route ($^{\bullet}OH$ desorption) better than γ-MnO_2-N. This was demonstrated by a smaller energy barrier needed to enable the $^{\bullet}OH \rightarrow NO_3^{\bullet}$ route for α-MnO_2-N in comparison with that for γ-MnO_2-N.

On the other hand, α-MnO_2 imparted $Mn^{2+/3+}$ and labile O, both of which were more adequate to disperse NO_3^- functionalities compared to those of γ-MnO_2. This led to higher N contents (via EA/XRF and XPS) and higher NO_3^- concentration (via XPS/XANES) in the resulting α-MnO_2-N in comparison with γ-MnO_2-N, all of which again could allow for the tentative conclusion that α-MnO_2 is the optimum architecture to proceed with the $^{\bullet}OH \rightarrow NO_3^{\bullet}$ route upon NO_3^- functionalization. Apparently, the $^{\bullet}OH \rightarrow NO_3^{\bullet}$ route could be activated by α-/γ-MnO_2-N surfaces to generate $^{\bullet}OH/^{\bullet}OOH/O_2^{\bullet-}/NO_2^{\bullet}{}_{SUP}/NO_3^{\bullet}{}_{SUP}$, as substantiated by EPR spectra observed/simulated. Of significance, the formation of $NO_3^{\bullet}{}_{SUP}$ via radical transfer from $^{\bullet}OH$ to NO_3^- was highly tangible and exothermic across α-/γ-MnO_2-N surfaces, as proved by EPR spectra observed/simulated and DFT calculations, respectively. Of additional significance, $NO_3^{\bullet}{}_{SUP}$ on α-/γ-MnO_2-N played a major role in decomposing phenol, as validated by scavenging and filtration runs.

Overall, α-MnO_2-N outperformed γ-MnO_2-N in decomposing phenol and textile wastewater with the prime utilization of $NO_3^{\bullet}{}_{SUP}$ species. The efficiency of $NO_3^{\bullet}{}_{SUP}$ on α-MnO_2-N in decomposing phenol or textile wastewater was higher than those of conventional $^{\bullet}OH$ and/or supported $SO_4^{\bullet-}$ species generated via radical interconversion of $^{\bullet}OH \leftrightarrow SO_4^{\bullet-}$ on Fe_2O_3 or NiO we discovered previously. This study has demonstrated the impact of $NO_3^{\bullet}{}_{SUP}$ as a potent degrader of aqueous contaminants yet opens an additional study on how to increase the amount of $NO_3^{\bullet}{}_{SUP}$ precursors (NO_3^-) deposited on the catalyst surface. This is an ongoing research performed in our laboratory.

■ ASSOCIATED CONTENT

Supporting Information

The Supporting Information is available free of charge at https://pubs.acs.org/doi/10.1021/jacsau.1c00124.

Properties of chemical species and/or radical quenchers; hyperfine splitting constants of spin adducts; HRTEM images, SAED/XRD patterns, XP spectra, *in situ* NH_3-DRIFT spectra, *in situ* NO/O_2-DRIFT spectra, EPR spectra, CO/CO_2 isotherms, H_2-TPR profiles, and computed surfaces for the catalysts; H_2O_2 scission profiles, phenol decomposition profiles, textile wastewater degradation profiles, fittings of reaction data to pseudo-first-order kinetic model, apparent reaction rate constants, and amounts of metal/nitrogen leached for the catalysts. (PDF)

■ AUTHOR INFORMATION

Corresponding Authors

Jongsik Kim − *Extreme Materials Research Center, Korea Institute of Science and Technology, Seoul 02792, South Korea*; orcid.org/0000-0003-2248-2576; Email: jkim40@kist.re.kr

Keunhong Jeong − *Department of Chemistry, Korea Military Academy, Seoul 01805, South Korea*; Email: doas1mind@kma.ac.kr

Authors

Yun Jeong Choe − *Extreme Materials Research Center, Korea Institute of Science and Technology, Seoul 02792, South Korea; Department of Materials Science and Engineering, Seoul National University, Seoul 08826, South Korea*

Sang Hoon Kim − *Extreme Materials Research Center, Korea Institute of Science and Technology, Seoul 02792, South Korea; Division of Nano and Information Technology, Korea Institute of Science and Technology School, University of Science and Technology, Daejeon 34113, South Korea*; orcid.org/0000-0002-5032-4658

In-Suk Choi − *Department of Materials Science and Engineering, Seoul National University, Seoul 08826, South Korea*; orcid.org/0000-0002-5933-7551

Complete contact information is available at: https://pubs.acs.org/10.1021/jacsau.1c00124

Author Contributions

[⊥]J.K. and Y.J.C. contributed equally. J.K. conceptualized the hypotheses and mechanisms, designed the experiments, refined and interpreted the data, and drafted the manuscript. Y.J.C. performed the experiments, refined and interpreted the data, and provided comments on the manuscript. S.H.K. and I.-S.C. provided comments on the manuscript. K.J. performed the calculations, refined and interpreted the data, and drafted the manuscript.

Notes

The authors declare no competing financial interest.

■ ACKNOWLEDGMENTS

We thank Ministry of Science and ICT and National Research Foundation of South Korea for providing a grant for this project (#NRF-2020R1A2C2004395). We are grateful to Korea Institute of Science and Technology (KIST) for supporting this project through Future R & D (#2E31191) and Young Fellow programs (#2E31192). We appreciate DYETEC for providing textile wastewater. We are thankful to SAMSUNG BLUETECH for helping commercialize the catalyst discovered in this study.

■ REFERENCES

(1) Pinkernell, U.; von Gunten, U. Bromate Minimization during Ozonation: Mechanistic Considerations. *Environ. Sci. Technol.* **2001**, 35 (12), 2525.

(2) Yuan, S.; Liao, P.; Alshawabkeh, A. N. Electrolytic Manipulation of Persulfate Reactivity by Iron Electrodes for Trichloroethylene Degradation in Groundwater. *Environ. Sci. Technol.* **2014**, *48* (1), 656.
(3) Antoniou, M. G.; de la Cruz, A. A.; Dionysiou, D. D. Intermediates and Reaction Pathways from the Degradation of Microcystin-LR with Sulfate Radicals. *Environ. Sci. Technol.* **2010**, *44* (19), 7238.
(4) Połczyński, P.; Jurczakowski, R.; Grochala, W. Stabilization and strong oxidizing properties of Ag (II) in a fluorine-free solvent. *Chem. Commun.* **2013**, *49* (68), 7480.
(5) Debnath, B.; Roy, A. S.; Kapri, S.; Bhattacharyya, S. Efficient Dye Degradation Catalyzed by Manganese Oxide Nanoparticles and the Role of Cation Valence. *ChemistrySelect* **2016**, *1* (14), 4265.
(6) Sun, Y.; Zhao, L.; Teng, Y. Insight into influence mechanisms of pyrite and vernadite on the degradation performance of 2,2′,5-trichlorodiphenyl in a pyrophosphate-chelated Fenton-like reaction. *Chem. Eng. J.* **2021**, *410*, 128345.
(7) Yang, J.; Ao, Z.; Wu, H.; Zhang, S. Immobilization of chitosan-templated MnO2 nanoparticles onto filter paper by redox method as a retrievable Fenton-like dip catalyst. *Chemosphere* **2021**, *268*, 128835.
(8) Xiao, R.; Ye, T.; Wei, Z.; Luo, S.; Yang, Z.; Spinney, R. Quantitative Structure-Activity Relationship (QSAR) for the Oxidation of Trace Organic Contaminants by Sulfate Radical. *Environ. Sci. Technol.* **2015**, *49* (22), 13394.
(9) Huie, R. E.; Herron, J. T. The rate constant for the reaction O_3 + NO_2 → O_2 + NO_3 over the temperature range 259−362 K. *Chem. Phys. Lett.* **1974**, *27* (3), 411.
(10) Musat, R.; Marignier, J. L.; Le Naour, C.; Denisov, S.; Venault, L.; Moisy, P.; Mostafavi, M. Pulse radiolysis study on the reactivity of $NO_3^•$ radical toward uranous (IV), hydrazinium nitrate and hydroxyl ammonium nitrate at room temperature and at 45 °C. *Phys. Chem. Chem. Phys.* **2020**, *22* (9), 5188.
(11) Musat, R.; Denisov, S. A.; Marignier, J.-L.; Mostafavi, M. Decoding the Three-Pronged Mechanism of $NO_3^•$ Radical Formation in HNO_3 Solutions at 22 and 80 °C Using Picosecond Pulse Radiolysis. *J. Phys. Chem. B* **2018**, *122* (7), 2121.
(12) Goldstein, S.; Rabani, J. Mechanism of Nitrite Formation by Nitrate Photolysis in Aqueous Solutions: The Role of Peroxynitrite, Nitrogen Dioxide, and Hydroxyl Radical. *J. Am. Chem. Soc.* **2007**, *129* (34), 10597.
(13) Barzaghi, P.; Herrmann, H. Kinetics and mechanisms of reactions of the nitrate radical ($NO_3^•$) with substituted phenols in aqueous solution. *Phys. Chem. Chem. Phys.* **2004**, *6* (23), 5379.
(14) Villegas-Guzman, P.; Hofer, F.; Silva-Agredo, J.; Torres-Palma, R. A. Role of sulfate, chloride, and nitrate anions on the degradation of fluoroquinolone antibiotics by photoelectro-Fenton. *Environ. Sci. Pollut. Res.* **2017**, *24* (36), 28175.
(15) Nakatani, N.; Hashimoto, N.; Shindo, H.; Yamamoto, M.; Kikkawa, M.; Sakugawa, H. Determination of photoformation rates and scavenging rate constants of hydroxyl radicals in natural waters using an automatic light irradiation and injection system. *Anal. Chim. Acta* **2007**, *581* (2), 260.
(16) Liu, Z.; Fang, Z.; Wang, L.; He, H.; Lin, M.-Z. Alpha radiolysis of nitric acid aqueous solution irradiated by ^{238}Pu source. *Nucl. Sci. Tech.* **2017**, *28* (4), 54.
(17) Chen, L.; Li, J.; Ge, M. Promotional Effect of Ce-doped V_2O_5-WO_3/TiO_2 with Low Vanadium Loadings for Selective Catalytic Reduction of NO_X by NH_3. *J. Phys. Chem. C* **2009**, *113* (50), 21177.
(18) Kim, J.; Kim, D. H.; Kwon, D. W.; Ha, H. P. Rational selection of $Fe_2V_4O_{13}$ over $FeVO_4$ as a preferred active site on Sb-promoted TiO_2 for catalytic NO_X reduction with NH_3. *Catal. Sci. Technol.* **2018**, *8* (18), 4774.
(19) Vinge, S. L.; Shaheen, S. W.; Sharpless, C. M.; Linden, K. G. Nitrate with benefits: optimizing radical production during UV water treatment. *Environ. Sci.: Water Res. Technol.* **2020**, *6* (4), 1163.
(20) Madsen, D.; Larsen, J.; Jensen, S. K.; Keiding, S. R.; Thøgersen, J. The Primary Photodynamics of Aqueous Nitrate: Formation of Peroxynitrite. *J. Am. Chem. Soc.* **2003**, *125* (50), 15571.
(21) Julian, R. R.; Beauchamp, J. L.; Goddard, W. A. Cooperative Salt Bridge Stabilization of Gas-Phase Zwitterions in Neutral Arginine Clusters. *J. Phys. Chem. A* **2002**, *106* (1), 32.
(22) Chen, C.; Wu, Z.; Zheng, S.; Wang, L.; Niu, X.; Fang, J. Comparative Study for Interactions of Sulfate Radical and Hydroxyl Radical with Phenol in the Presence of Nitrite. *Environ. Sci. Technol.* **2020**, *54* (13), 8455.
(23) Bartberger, M. D.; Liu, W.; Ford, E.; Miranda, K. M.; Switzer, C.; Fukuto, J. M.; Farmer, P. J.; Wink, D. A.; Houk, K. N. The reduction potential of nitric oxide (NO) and its importance to NO biochemistry. *Proc. Natl. Acad. Sci. U. S. A.* **2002**, *99* (17), 10958.
(24) Samuel, E. L. G.; Marcano, D. C.; Berka, V.; Bitner, B. R.; Wu, G.; Potter, A.; Fabian, R. H.; Pautler, R. G.; Kent, T. A.; Tsai, A.-L.; et al. Highly efficient conversion of superoxide to oxygen using hydrophilic carbon clusters. *Proc. Natl. Acad. Sci. U. S. A.* **2015**, *112* (8), 2343.
(25) Keen, O. S.; Love, N. G.; Linden, K. G. The role of effluent nitrate in trace organic chemical oxidation during UV disinfection. *Water Res.* **2012**, *46* (16), 5224.
(26) Kim, J.; Choe, Y. J.; Kim, S. H.; Jeong, K. Enhancing the decomposition of refractory contaminants on SO_4^{2-}-functionalized iron oxide to accommodate surface $SO_4^{•-}$ generated via radical transfer from $^•OH$. *Appl. Catal., B* **2019**, *252*, 62.
(27) Choe, Y. J.; Kim, J.-S.; Kim, H.; Kim, J. Open Ni site coupled with SO_4^{2-} functionality to prompt the radical interconversion of $^•OH$ ↔ $SO_4^{•-}$ exploited to decompose refractory pollutants. *Chem. Eng. J.* **2020**, *400*, 125971.
(28) Kim, J.; Choe, Y. J.; Kim, S. H. Tailoring Lewis acidic metals and SO_4^{2-} functionalities on bimetallic Mn-Fe oxo-spinels to exploit supported $SO_4^{•-}$ in aqueous pollutant fragmentation. *Chem. Eng. J.* **2021**, *413*, 127550.
(29) Zhao, J.; Yang, J.; Ma, J. Mn (II)-enhanced oxidation of benzoic acid by Fe (III)/H_2O_2 system. *Chem. Eng. J.* **2014**, *239*, 171.
(30) Hansard, S. P.; Easter, H. D.; Voelker, B. M. Rapid Reaction of Nanomolar Mn (II) with Superoxide Radical in Seawater and Simulated Freshwater. *Environ. Sci. Technol.* **2011**, *45* (7), 2811.
(31) Schneider, W. F. Qualitative Differences in the Adsorption Chemistry of Acidic (CO_2, SO_X) and Amphiphilic (NO_X) Species on the Alkaline Earth Oxides. *J. Phys. Chem. B* **2004**, *108* (1), 273.
(32) Gonzalez, C. M.; Hernandez, J.; Peralta-Videa, J. R.; Botez, C. E.; Parsons, J. G.; Gardea-Torresdey, J. L. Sorption kinetic study of selenite and selenate onto a high and low pressure aged iron oxide nanomaterial. *J. Hazard. Mater.* **2012**, *211*−*212*, 138.
(33) Wang, F.; Dai, H.; Deng, J.; Bai, G.; Ji, K.; Liu, Y. Manganese Oxides with Rod-, Wire-, Tube-, and Flower-Like Morphologies: Highly Effective Catalysts for the Removal of Toluene. *Environ. Sci. Technol.* **2012**, *46* (7), 4034.
(34) Li, L.; Wu, Y.; Hou, X.; Chu, B.; Nan, B.; Qin, Q.; Fan, M.; Sun, C.; Li, B.; Dong, L.; et al. Investigation of Two-Phase Intergrowth and Coexistence in Mn−Ce−Ti−O Catalysts for the Selective Catalytic Reduction of NO with NH_3: Structure-Activity Relationship and Reaction Mechanism. *Ind. Eng. Chem. Res.* **2019**, *58* (2), 849.
(35) Helali, Z.; Jedidi, A.; Syzgantseva, O. A.; Calatayud, M.; Minot, C. Scaling reducibility of metal oxides. *Theor. Chem. Acc.* **2017**, *136* (9), 100.
(36) Zhu, B.; Fang, Q.; Sun, Y.; Yin, S.; Li, G.; Zi, Z.; Ge, T.; Zhu, Z.; Zhang, M.; Li, J. Adsorption properties of NO, NH_3, and O_2 over β-MnO_2 (110) surface. *J. Mater. Sci.* **2018**, *53* (16), 11500.
(37) Liu, L.; Zheng, C.; Wang, J.; Zhang, Y.; Gao, X.; Cen, K. NO Adsorption and Oxidation on Mn Doped CeO_2 (111) Surfaces: A DFT+U Study. *Aerosol Air Qual. Res.* **2018**, *18* (4), 1080.
(38) Yuan, H.; Sun, N.; Chen, J.; Jin, J.; Wang, H.; Hu, P. Insight into the NH_3-Assisted Selective Catalytic Reduction of NO on β-MnO_2 (110): Reaction Mechanism, Activity Descriptor, and Evolution from a Pristine State to a Steady State. *ACS Catal.* **2018**, *8* (10), 9269.
(39) Kim, J.; Lee, S.; Ha, H. P. Supercritical Carbon Dioxide Extraction-Mediated Amendment of a Manganese Oxide Surface

https://doi.org/10.1021/jacsau.1c00124
JACS Au 2021, 1, 1158−1177

Desired to Selectively Transform Nitrogen Oxides and/or Ammonia. *ACS Catal.* **2021**, *11* (2), 767.
(40) Borgmann, S. Electrochemical quantification of reactive oxygen and nitrogen: challenges and opportunities. *Anal. Bioanal. Chem.* **2009**, *394* (1), 95.
(41) Nawaz, F.; Xie, Y.; Xiao, J.; Cao, H.; Ghazi, Z. A.; Guo, Z.; Chen, Y. The influence of the substituent on the phenol oxidation rate and reactive species in cubic MnO_2 catalytic ozonation. *Catal. Sci. Technol.* **2016**, *6* (21), 7875.
(42) Xu, H.; Yan, N.; Qu, Z.; Liu, W.; Mei, J.; Huang, W.; Zhao, S. Gaseous Heterogeneous Catalytic Reactions over Mn-Based Oxides for Environmental Applications: A Critical Review. *Environ. Sci. Technol.* **2017**, *51* (16), 8879.
(43) Li, Y.-F.; Zhu, S.-C.; Liu, Z.-P. Reaction Network of Layer-to-Tunnel Transition of MnO_2. *J. Am. Chem. Soc.* **2016**, *138* (16), 5371.
(44) Hayashi, E.; Yamaguchi, Y.; Kamata, K.; Tsunoda, N.; Kumagai, Y.; Oba, F.; Hara, M. Effect of MnO_2 Crystal Structure on Aerobic Oxidation of 5-Hydroxymethylfurfural to 2,5-Furandicarboxylic Acid. *J. Am. Chem. Soc.* **2019**, *141* (2), 890.
(45) Bi, R.; Liu, G.; Zeng, C.; Wang, X.; Zhang, L.; Qiao, S.-Z. 3D Hollow α-MnO_2 Framework as an Efficient Electrocatalyst for Lithium−Oxygen Batteries. *Small* **2019**, *15* (10), 1804958.
(46) Ren, Y.; Armstrong, A. R.; Jiao, F.; Bruce, P. G. Influence of Size on the Rate of Mesoporous Electrodes for Lithium Batteries. *J. Am. Chem. Soc.* **2010**, *132* (3), 996.
(47) Dong, Y.; Li, K.; Jiang, P.; Wang, G.; Miao, H.; Zhang, J.; Zhang, C. Simple hydrothermal preparation of α-, β-, and γ-MnO_2 and phase sensitivity in catalytic ozonation. *RSC Adv.* **2014**, *4* (74), 39167.
(48) Saputra, E.; Muhammad, S.; Sun, H.; Ang, H. M.; Tadé, M. O.; Wang, S. Different Crystallographic One-dimensional MnO_2 Nanomaterials and Their Superior Performance in Catalytic Phenol Degradation. *Environ. Sci. Technol.* **2013**, *47* (11), 5882.
(49) Dong, Y.; Yang, H.; He, K.; Song, S.; Zhang, A. β-MnO_2 nanowires: A novel ozonation catalyst for water treatment. *Appl. Catal., B* **2009**, *85* (3), 155.
(50) Liu, W.; Zhang, X.; Huang, Y.; Jiang, B.; Chang, Z.; Xu, C.; Kang, F. β-MnO_2 with proton conversion mechanism in rechargeable zinc ion battery. *J. Energy Chem.* **2021**, *56*, 365.
(51) Meng, H.; Nie, C.; Li, W.; Duan, X.; Lai, B.; Ao, Z.; Wang, S.; An, T. Insight into the effect of lignocellulosic biomass source on the performance of biochar as persulfate activator for aqueous organic pollutants remediation: Epicarp and mesocarp of citrus peels as examples. *J. Hazard. Mater.* **2020**, *399*, 123043.
(52) Mo, S.; Zhang, Q.; Li, J.; Sun, Y.; Ren, Q.; Zou, S.; Zhang, Q.; Lu, J.; Fu, M.; Mo, D.; et al. Highly efficient mesoporous MnO_2 catalysts for the total toluene oxidation: Oxygen-Vacancy defect engineering and involved intermediates using *in situ* DRIFTS. *Appl. Catal., B* **2020**, *264*, 118464.
(53) Borgschulte, A.; Callini, E.; Stadie, N.; Arroyo, Y.; Rossell, M. D.; Erni, R.; Geerlings, H.; Züttel, A.; Ferri, D. Manipulating the reaction path of the CO_2 hydrogenation reaction in molecular sieves. *Catal. Sci. Technol.* **2015**, *5* (9), 4613.
(54) Chen, L.; Liu, Y.; Fang, X.; Cheng, Y. Simple strategy for the construction of oxygen vacancies on α-MnO_2 catalyst to improve toluene catalytic oxidation. *J. Hazard. Mater.* **2021**, *409*, 125020.
(55) Liu, Y.; Zhang, P. Removing Surface Hydroxyl Groups of Ce-Modified MnO_2 To Significantly Improve Its Stability for Gaseous Ozone Decomposition. *J. Phys. Chem. C* **2017**, *121* (42), 23488.
(56) Huang, Y.; Jia, Y.; Shen, K.; Hou, R.; Zhang, Y.; Hou, L. a. Degradation of gaseous unsymmetrical dimethylhydrazine by vacuum ultraviolet coupled with MnO_2. *New J. Chem.* **2021**, *45* (3), 1194.
(57) Kakazey, M.; Ivanova, N.; Boldurev, Y.; Ivanov, S.; Sokolsky, G.; Gonzalez-Rodriguez, J. G.; Vlasova, M. Electron paramagnetic resonance in MnO_2 powders and comparative estimation of electric characteristics of power sources based on them in the MnO_2−Zn system. *J. Power Sources* **2003**, *114* (1), 170.
(58) Yang, W.; Peng, Y.; Wang, Y.; Wang, Y.; Liu, H.; Su, Z. a.; Yang, W.; Chen, J.; Si, W.; Li, J. Controllable redox-induced in-situ growth of MnO_2 over Mn_2O_3 for toluene oxidation: Active heterostructure interfaces. *Appl. Catal., B* **2020**, *278*, 119279.
(59) Duan, J.; Higuchi, M.; Krishna, R.; Kiyonaga, T.; Tsutsumi, Y.; Sato, Y.; Kubota, Y.; Takata, M.; Kitagawa, S. High $CO_2/N_2/O_2/CO$ separation in a chemically robust porous coordination polymer with low binding energy. *Chem. Sci.* **2014**, *5* (2), 660.
(60) Kim, M.; Kim, S. H.; Lee, J.-H.; Kim, J. Unravelling lewis acidic and reductive characters of normal and inverse nickel-cobalt thiospinels in directing catalytic H_2O_2 cleavage. *J. Hazard. Mater.* **2020**, *392*, 122347.
(61) Tovar, T. M.; Zhao, J.; Nunn, W. T.; Barton, H. F.; Peterson, G. W.; Parsons, G. N.; LeVan, M. D. Diffusion of CO_2 in Large Crystals of Cu-BTC MOF. *J. Am. Chem. Soc.* **2016**, *138* (36), 11449.
(62) Alkhabbaz, M. A.; Bollini, P.; Foo, G. S.; Sievers, C.; Jones, C. W. Important Roles of Enthalpic and Entropic Contributions to CO_2 Capture from Simulated Flue Gas and Ambient Air Using Mesoporous Silica Grafted Amines. *J. Am. Chem. Soc.* **2014**, *136* (38), 13170.
(63) Sillar, K.; Kundu, A.; Sauer, J. Ab Initio Adsorption Isotherms for Molecules with Lateral Interactions: CO_2 in Metal−Organic Frameworks. *J. Phys. Chem. C* **2017**, *121* (23), 12789.
(64) Pulido, A.; Delgado, M. R.; Bludský, O.; Rubeš, M.; Nachtigall, P.; Areán, C. O. Combined DFT/CC and IR spectroscopic studies on carbon dioxide adsorption on the zeolite H-FER. *Energy Environ. Sci.* **2009**, *2* (11), 1187.
(65) Lee, S.; Lee, J. H.; Kim, J. C.; Lee, S.; Kwak, S. K.; Choe, W. Porous Zr_6L_3 Metallocage with Synergetic Binding Centers for CO_2. *ACS Appl. Mater. Interfaces* **2018**, *10* (10), 8685.
(66) Kim, J.; Ho Kim, D.; Ha, H. P. Investigating multi-functional traits of metal-substituted vanadate catalysts in expediting NO_X reduction and poison degradation at low temperatures. *J. Hazard. Mater.* **2020**, *397*, 122671.
(67) Kim, J.; Nam, K. B.; Ha, H. P. Comparative study of HSO_A^-/SO_A^{2-} versus $H_{3-B}PO_4^{B-}$ functionalities anchored on TiO_2-supported antimony oxide-vanadium oxide-cerium oxide composites for low-temperature NO_X activation. *J. Hazard. Mater.* **2021**, *416*, 125780.
(68) An, H. J.; Kim, D. H.; Ha, H. P.; Kim, J. NO_X reduction consequences of lanthanide-substituted vanadates functionalized with S or P poisons under oxidative environments. *J. Mater. Chem. A* **2021**, *9* (13), 8350.
(69) Choe, Y. J.; Byun, J. Y.; Kim, S. H.; Kim, J. Fe_3S_4/Fe_7S_8-promoted degradation of phenol via heterogeneous, catalytic H_2O_2 scission mediated by S-modified surface Fe^{2+} species. *Appl. Catal., B* **2018**, *233*, 272.
(70) He, W.; Kim, H.-K.; Wamer, W. G.; Melka, D.; Callahan, J. H.; Yin, J.-J. Photogenerated Charge Carriers and Reactive Oxygen Species in ZnO/Au Hybrid Nanostructures with Enhanced Photocatalytic and Antibacterial Activity. *J. Am. Chem. Soc.* **2014**, *136* (2), 750.
(71) Huang, S.; Xu, Y.; Zhou, T.; Xie, M.; Ma, Y.; Liu, Q.; Jing, L.; Xu, H.; Li, H. Constructing magnetic catalysts with *in-situ* solid-liquid interfacial photo-Fenton-like reaction over Ag_3PO_4@$NiFe_2O_4$ composites. *Appl. Catal., B* **2018**, *225*, 40.
(72) He, X.; Sun, B.; He, M.; Chi, H.; Wang, Z.; Zhang, W.; Ma, J. Highly efficient simultaneous catalytic degradation and defluorination of perfluorooctanoic acid by the H_2O_2-carbon/MnO_2 system generating $O_2^{\bullet-}$ and $^{\bullet}OH$ synchronously. *Appl. Catal., B* **2020**, *277*, 119219.
(73) Xiao, J.; Rabeah, J.; Yang, J.; Xie, Y.; Cao, H.; Brückner, A. Fast Electron Transfer and $^{\bullet}OH$ Formation: Key Features for High Activity in Visible-Light-Driven Ozonation with C_3N_4 Catalysts. *ACS Catal.* **2017**, *7* (9), 6198.
(74) Villamena, F. A.; Merle, J. K.; Hadad, C. M.; Zweier, J. L. Superoxide Radical Anion Adduct of 5,5-Dimethyl-1-pyrroline N-Oxide (DMPO). 1. The Thermodynamics of Formation and Its Acidity. *J. Phys. Chem. A* **2005**, *109* (27), 6083.
(75) Lawrence, C. C.; Bennati, M.; Obias, H. V.; Bar, G.; Griffin, R. G.; Stubbe, J. High-field EPR detection of a disulfide radical anion in the reduction of cytidine 5′-diphosphate by the E441Q R1 mutant of

https://doi.org/10.1021/jacsau.1c00124
JACS Au 2021, 1, 1158−1177

Escherichia coli ribonucleotide reductase. *Proc. Natl. Acad. Sci. U. S. A.* **1999**, *96* (16), 8979.
(76) Prisner, T.; Rohrer, M.; MacMillan, F. PULSED EPR SPECTROSCOPY: Biological Applications. *Annu. Rev. Phys. Chem.* **2001**, *52* (1), 279.
(77) Ren, J. Y.; Chang, C. Q.; Fung, P. C. W.; Shen, J. G.; Chan, F. H. Y. Free radical EPR spectroscopy analysis using blind source separation. *J. Magn. Reson.* **2004**, *166* (1), 82.
(78) Bautista, F. M.; Blanco, A.; Campelo, J. M.; Garcia, A.; Luna, D.; Marinas, J. M.; Romero, A. A. Continuous flow toluene methylation over $AlPO_4$ and $AlPO_4$-Al_2O_3 catalysts. *Catal. Lett.* **1994**, *26* (1), 159.
(79) Kim, J.; Go, D. B.; Hicks, J. C. Synergistic effects of plasma–catalyst interactions for CH_4 activation. *Phys. Chem. Chem. Phys.* **2017**, *19* (20), 13010.
(80) Kozmér, Z.; Arany, E.; Alapi, T.; Takács, E.; Wojnárovits, L.; Dombi, A. Determination of the rate constant of hydroperoxyl radical reaction with phenol. *Radiat. Phys. Chem.* **2014**, *102*, 135.
(81) Wang, B.; Wang, M.; Han, L.; Hou, Y.; Bao, W.; Zhang, C.; Feng, G.; Chang, L.; Huang, Z.; Wang, J. Improved Activity and SO_2 Resistance by Sm-Modulated Redox of $MnCeSmTiO_X$ Mesoporous Amorphous Oxides for Low-Temperature NH_3-SCR of NO. *ACS Catal.* **2020**, *10* (16), 9034.
(82) Wen, T.; Zhao, Y.; Zhang, T.; Xiong, B.; Hu, H.; Zhang, Q.; Song, S. Effect of anions species on copper removal from wastewater by using mechanically activated calcium carbonate. *Chemosphere* **2019**, *230*, 127.
(83) Rodriguez, J. A.; Jirsak, T.; Liu, G.; Hrbek, J.; Dvorak, J.; Maiti, A. Chemistry of NO_2 on Oxide Surfaces: Formation of NO_3 on TiO_2 (110) and NO_2 ↔ O Vacancy Interactions. *J. Am. Chem. Soc.* **2001**, *123* (39), 9597.
(84) Szanyi, J.; Kwak, J. H.; Burton, S.; Rodriguez, J. A.; Peden, C. H. F. Characterization of NO_X species in dehydrated and hydrated Na- and Ba-Y, FAU zeolites formed in NO_2 adsorption. *J. Electron Spectrosc. Relat. Phenom.* **2006**, *150* (2), 164.
(85) Makino, K.; Hagi, A.; Ide, H.; Murakami, A.; Nishi, M. Mechanistic studies on the formation of aminoxyl radicals from 5,5-dimethyl-1-pyrroline-N-oxide in Fenton systems. Characterization of key precursors giving rise to background ESR signals. *Can. J. Chem.* **1992**, *70* (11), 2818.
(86) Feng, Y.; Wu, D.; Li, H.; Bai, J.; Hu, Y.; Liao, C.; Li, X.-y.; Shih, K. Activation of Persulfates Using Siderite as a Source of Ferrous Ions: Sulfate Radical Production, Stoichiometric Efficiency, and Implications. *ACS Sustainable Chem. Eng.* **2018**, *6* (3), 3624.
(87) Chávez, A. M.; Gimeno, O.; Rey, A.; Pliego, G.; Oropesa, A. L.; Álvarez, P. M.; Beltrán, F. J. Treatment of highly polluted industrial wastewater by means of sequential aerobic biological oxidation-ozone based AOPs. *Chem. Eng. J.* **2019**, *361*, 89.
(88) San Sebastián Martinez, N.; Fernández, J. F.; Segura, X. F.; Ferrer, A. S. Pre-oxidation of an extremely polluted industrial wastewater by the Fenton's reagent. *J. Hazard. Mater.* **2003**, *101* (3), 315.
(89) Zhang, G.; He, X.; Nadagouda, M. N.; O'Shea, K. E.; Dionysiou, D. D. The effect of basic pH and carbonate ion on the mechanism of photocatalytic destruction of cylindrospermopsin. *Water Res.* **2015**, *73*, 353.
(90) Liu, Y.; He, X.; Duan, X.; Fu, Y.; Dionysiou, D. D. Photochemical degradation of oxytetracycline: Influence of pH and role of carbonate radical. *Chem. Eng. J.* **2015**, *276*, 113.

https://doi.org/10.1021/jacsau.1c00124
JACS Au 2021, 1, 1158–1177